A bar-joint model based on the corrected resistive force theory for artificial flagellated micro-swimmers propelled by acoustic waves

Bioinspiration & Biomimetics

OPEN ACCESS

RECEIVED
9 November 2022

REVISED
14 February 2023

ACCEPTED FOR PUBLICATION
23 February 2023

PUBLISHED
13 March 2023

PAPER

A bar-joint model based on the corrected resistive force theory for artificial flagellated micro-swimmers propelled by acoustic waves

Jinan Liu[1], **Yiqiang Fu**[1], **Xiongjun Liu**[2] and **Haihui Ruan**[1,*]

[1] Research Center for Fluid-Structure Interactions, Department of Mechanical Engineering, The Hong Kong Polytechnic University, Hung Hom, Kowloon, Hong Kong, People's Republic of China
[2] State Key Laboratory for Advanced Metals and Materials, University of Science and Technology Beijing, Beijing 100083, People's Republic of China
[*] Author to whom any correspondence should be addressed.

E-mail: haihui.ruan@polyu.edu.hk

Keywords: artificial micro-swimmer, acoustic actuation, resistive force theory, propulsion

Supplementary material for this article is available online

Abstract

In this work, we proposed a bar-joint model based on the corrected resistive force theory (CRFT) for studying artificial flagellated micro-swimmers (AFMSs) propelled by acoustic waves in a two-dimensional (2D) flow field or with a rectangular cross-section. Note that the classical resistive-force theory for 3D cylindrical flagellum leads to over 90% deviation in terminal velocity from those of 2D fluid-structure interaction (FSI) simulations, while the proposed CRFT bar-joint model can reduce the deviation to below 5%; hence, it enables a reliable prediction of the 2D locomotion of an acoustically actuated AFMS with a rectangular cross-section, which is the case in some experiments. Introduced in the CRFT is a single correction factor K determined by comparing the linear terminal velocities under acoustic actuation obtained from the CRFT with those from simulations. After the determination of K, detailed comparisons of trajectories between the CRFT-based bar-joint AFMS model and the FSI simulation were presented, exhibiting an excellent consistency. Finally, a numerical demonstration of the purely acoustic or magneto-acoustic steering of an AFMS based on the CRFT was presented, which can be one of the choices for future AFMS-based precision therapy.

1. Introduction

1.1. Background

An artificial micro-swimmer normally refers to an object synthesized at the microscopic scale [1, 2] and capable of interacting with a fluidic environment to achieve locomotion. While natural micro-swimmers, i.e. microorganisms, have been studied since the invention of Leeuwenhoek's microscope in the 17th century, artificial micro-swimmers were not thought possible until Richard Feynman's famous lecture [3] on nanotechnology in 1959. Since then, people have fantasized about tiny untethered robots [4] to kill bacteria and implement targeted therapy *in vivo*. For example, a swarm of micro-swimmers actuated by acoustic power can swim along the intestinal tract to kill the cancer cells by generating heat under an alternated magnetic field (i.e. magnetic thermotherapy), as illustrated in figure 1. Nevertheless, these tasks are still very challenging, and most of the achievements are limited to laboratory studies [5, 6] where the micro-robots appear in diverse structures, such as bubbles [7, 8], nanorods [9, 10], helical filaments [11, 12], and flagella [13, 14]. In this work, we focus on artificial flagellated micro-swimmers (AFMSs).

An AFMS usually consists of a relatively rigid head and a flexible tail, as shown in the inset of figure 1, where the tail is customarily called a flagellum in microbiology [15]. We focus on the flagellated structure, especially the sperm-like one, because it is easy to fabricate through 3D printing [14] and is suitable for medical applications due to the potential of cargo transportation by its head [16]. Various actuation strategies have been proposed for artificial micro-swimmers, which can be classified into two categories

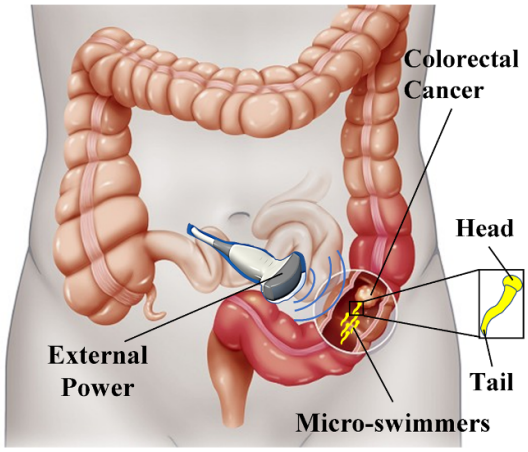

Figure 1. Schematic of a medical application of AFMSs.

[17]: the self-propulsion approaches, e.g. the catalytic reactions [18], and external actuation approaches, such as optical [19], thermal [20], magnetic [21], and acoustic actuation [22]. For AFMSs and considering medical applications, the acoustic and magnetic actuations are the most suitable because they are tissue- and circulation-friendly and have been employed in diagnosis and therapies [23]. Here we choose acoustic excitations for propulsion and navigation and also consider magnetic power to assist turning.

1.2. Micro-swimmer models and their verification

It is noted that the inertia of flagella and surrounding fluids can be ignored because the Reynolds number is sufficiently low at the microscale and when the dynamic response is away from resonance [24]. In a low Reynolds number (LRN) regime, the Navier–Stokes equation can be recast into the linear Stokes equation [25] and the linearity of the Stokes equation leads to the so-called Purcell's scallop theorem [26] which forbids objects with a reciprocal motion from moving. Instead, a traveling wave in a flagellum can generate net propulsion [27]; hence, whipping the flagellum of a micro-swimmer can propel itself forward. One may note that the strong acoustic streaming around the sharp edges is a well-established mechanism for propelling acoustically actuated swimmers [28, 29]. To simplify the swimming problem, as described by Liu and Ruan [24], the effect of actuation (e.g. an acoustic power) is simplified to actuation forces and torques on the head of a flagellated micro-swimmer, which leads to flagellum wiggling and propulsion. However, the expressions for fluid forces on a solid body are normally so complicated that numerical simulations are necessary to predict the locomotion [30]. Fortunately, if a body is slender (i.e. the ratio of the characteristic width to length is less than 0.1 [31]), an asymptotic expression in terms of the slenderness can be obtained, known as the slender body theory (SBT) [32–36]. However, the SBT is still too complex to be applied in most cases, because the interactions between different parts of the body have to be considered based on the SBT. If omitting these interactions and only considering the drags, i.e. each segment of a slender flagellum independently experiences resistance to its motion, the SBT is simplified into the resistive-force theory (RFT) [35, 37, 38].

Based on the RFT and the balance of the drag and elastic forces, Machin [39] proposed the first-order governing equation for a uniform flagellum. His work was followed by Wiggins and Goldstein [40] who established the so-called hyper-diffusion equation to describe an AFMS. Then, the propulsive force generated by whipping an elastic filament was experimentally verified based on the head movement [41]. The partial differential equations (PDEs) of a variable cross-section flagellum were proposed by Singh and Yadava [42]. Kaynak *et al* [14] first reported the fabrication of such sperm-like micro-swimmers and observed their swimming under the actuation of acoustic waves. Liu and Ruan [24] investigated the corresponding swimming mechanisms by assuming that the swing of the head arising from the acoustic actuation leads to the whipping of the flagellum and that the interaction between the flagellum and its surrounding fluid can generate propulsion. They employed the Galerkin method [43] to solve the governing equations and exhibited the results consistent with the experimental ones. It should be noted that the models of the AFMS are usually one-dimensional (1D) [6], which confines the swimmer's motion to a straight line. Considering the need for manipulation or steering in applications, such a 1D model is insufficient. Establishing at least a two-dimensional (2D) AFMS model to address plane motion is therefore indispensable.

One may derive the 2D governing PDEs of a flagellum via Hamilton's principle [44] if the dynamic profile of the flagellum is a known function [45]. Unfortunately, in swimming the wiggling profile of a flagellum is not ad hoc. In addition, a flagellum becomes curved in turning [46], bringing about geometric nonlinearly, and the influence of the rigid-body motion further increases the nonlinearity of problem. Therefore, a discrete flagellum model was developed to solve the 2D swimming problem. Inspired by Purcell's three-link swimmer [26], a flexible flagellum has been modeled by using multiple rigid bars linked by flexible joints (aka. the bar-joint models) [47], which intrinsically fulfills the inextensible constraints of a flexible tail [48, 49]. Moreau *et al* [50] compared the classical continuum model with the bar-joint model and demonstrated that the latter could achieve better numerical performance.

However, these models were not verified by simulations or experiments.

It is generally nontrivial to verify and correct micro-swimmer models experimentally because geometries and material properties are often uncertain (or undermined in literature). In addition, the wiggling profile of a flagellum is difficult to capture under a microscope. Hence, numerical simulations dealing with fluid-structure interactions (FSIs), which are usually based on the finite element method (FEM), were more desirable to verify a simplified micro-swimmer model. Rorai *et al* [31] studied a sperm-like micro-swimmer in a 3D infinite domain by FEM, and demonstrated an excellent agreement between the SBT and the FSI simulations in terms of the propulsive matrix coefficients. Nevertheless, the dynamic motion of the flagellum was specified *a priori*, and the swimmer for each time was fixed, i.e. the elasticity of the flagellum and the resultant rigid-body motion were not investigated. Curatolo and Teresi [51] employed the automatic remeshing technique [52, 53] to couple the structure's rigid-body motion with FSI simulations for a fish-like swimmer. However, they did not compare their simulation results with those of RFT or SBT.

Undoubtedly, differences exist between the results of FSI simulations and the RFT or SBT models due to various reasons. For example, the RFT and SBT can hardly address fluid problems around a flagellum tip or a head-flagellum joint [31]. The fluid force exerted on a head is also difficult to estimate because the head is normally neither a sphere nor a slender body. Most importantly, the RFT and SBT are initially established for a slender cylindrical body, but the flagellum in 2D simulations (considering that 3D simulations are computationally too demanding) approximates a slender body with rectangular cross-sections, which is often the case in experiments (e.g. [14]). In addition, the most prevailing AFMS fabrication is based on layer-by-layer photocuring (i.e. 3D printing) [54], which leads to flagella with rectangular cross-sections and hence, the need for modifying SBT and RFT for them.

The SBT for arbitrary cross-section has been developed by adding a dimensionless coefficient tensor **K** [55], depending only on the cross-sectional geometry, to the fluid velocity field. Borker and Koch [56] extended this method to particle dynamics in shear flows and determined the magnitudes of components of **K** through FSI simulations. However, such a geometry-dependent **K** is insufficient to predict the locomotion of an AFMS because of the aforementioned complexities. In particular, when dealing with AFMS turning, the corrected SBT is still very difficult to solve [57]. Hence, we argue that a correction to RFT, considering both the effect of non-circular cross-section and the match of the linear terminal speed with the corresponding FSI simulation, may be a better strategy of approximation.

1.3. Arrangement of the following sections

In the subsequent sections, we will follow the above thought to develop the governing equations of an AFMS based on a bar-joint model and a corrected resistive-force theory (CRFT) for AFMS with rectangular cross-sections. In section 2, we will derive the expressions of CRFT and the governing equations of a bar-joint model. In section 3, we will first state the swimming problem and corresponding FSI simulations, then examples of convergence analyses of FSI simulation will be presented. After that, the correction factor K is determined in terms of different geometrical, materials, and acoustic-actuation parameters. Comparisons of swimmer's trajectories between the CRFT-based bar-joint model and the FSI simulation will then be presented as a verification of our theory, and a demonstration of the acoustic or magneto-acoustic steering strategy for the AFMS will be shown as the examples of applications. Finally, we will conclude the results of this research in section 4.

2. Modeling of AFMS

2.1. Correction to the RFT

The correction of SBT for the case of non-circular cross-section has been developed in [55]. Here we briefly introduce the concept and then simplify it to a more convenient form, i.e. the CRFT. In a LRN regime, the Navier–Stokes equations of fluid reduce to the linear Stokes equations [25] given by:

$$-\nabla p+\mu\nabla^2\mathbf{u}=0,\ \nabla\cdot\mathbf{u}=0, \qquad (1a,b)$$

where $\mathbf{u}$ and p are the velocity and pressure fields of a fluid, respectively, and μ the dynamic viscosity. Considering a slender body of unit length, let $\mathbf{S}(s)=\left[S_{\parallel}(s),S_{\perp}(s)\right]^{\mathrm{T}}$ be the distribution of Stokeslets [58], where the superscript T denotes transpose and $0\leqslant s\leqslant 1$ is the arclength along the body centerline. Applying the linear superposition method (equation (1*a*,*b*) are linear) to solve the fluid field and pressure distribution, the total fluid force $\mathbf{F}_f$ acting on a flagellum of unit length can be obtained as:

$$\mathbf{F}_f=-8\pi\mu\int_0^1\mathbf{S}(s)\,\mathrm{d}s. \qquad (2)$$

Let $\mathbf{P}(s)$ and $\kappa(s)$ be the coordinates and the half-width of the body at the position s along the body centerline, where $\kappa(s)$ also indicates how slender the body is. If κ is sufficiently small and the cross-section

is circular, one can obtain the classical expression of **S** based on the SBT [35]:

$$\mathbf{S}(s)=\frac{2\mathbf{I}-\hat{\mathbf{x}}(s)\hat{\mathbf{x}}(s)}{4\ln\kappa(s)}\cdot\left\{\mathbf{u}(s)-\mathbf{V}(s)+S_{\perp}(s)\hat{\mathbf{y}}(s)\right.$$
$$+\ln\left[4s(1-s)\right]\mathbf{S}(s)+S_{\parallel}(s)\left\{\ln\left[4s(1-s)\right]-2\right\}\hat{\mathbf{x}}(s)$$
$$\left.+\int_{-s}^{1-s}\left[\frac{\mathbf{S}(s+\delta)}{|\mathbf{P}_{s\delta}|}-\frac{\mathbf{S}(s)}{|\delta|}+\frac{\mathbf{P}_{s\delta}\mathbf{P}_{s\delta}\cdot\mathbf{S}(s+\delta)}{|\mathbf{P}_{s\delta}|^{3}}\right.\right.$$
$$\left.\left.-\frac{S_{\parallel}(s)\delta^{2}\hat{\mathbf{x}}(s)}{|\delta|^{3}}\right]\mathrm{d}\delta\right\} \tag{3}$$

where $\hat{\mathbf{x}}(s)$ and $\hat{\mathbf{y}}(s)$ are orthogonal unit vectors that are tangential and normal to the body centerline, respectively, **I** the identity matrix, $\mathbf{P}_{s\delta}=\mathbf{P}(s)-\mathbf{P}(s+\delta)$ the distance vector, and $\mathbf{V}(s)$ the local translational velocity of the body.

To deal with arbitrary flagellum cross-sections or 2D problems (i.e. with rectangular cross-sections), we follow the method proposed in [55] to introduce a dimensionless coefficient tensor **K** to the expression of fluid velocity field. Based on the SBT for circular flagellum cross-section, the relative fluid velocity field can be expressed as: $\mathbf{U}=\mathbf{C}\cdot\mathbf{S}$, where $\mathbf{U}(s)=\mathbf{u}(s)-\mathbf{V}(s)$ represents the relative velocity of the fluid with respect to the flagellum part at point s. For non-circular ones, it is assumed that the relative fluid velocity for the non-circular case is: $\mathbf{U}=(\mathbf{C}+\mathbf{K})\cdot\mathbf{S}$, where **C** is the resistive tensor, and the Stokeslets **S** is still based on the expression for a slender body with a circular cross-section. Note that the revised expression of **U** can still meet the zero-divergence condition for fluid velocity (i.e. equation (1b)) as long as **K** is a symmetric tensor with zero divergence.

In [55], **K** depends only on the shape of the cross-section, which can be directly estimated for some special shapes without performing FSI simulations. Nevertheless, in most cases, FSI simulations are required to determine **K** because the dynamics of a solid body (e.g. the wiggling profile of a flagellum), which affects **U** and **K**, cannot be determined *a priori*, as reported by Borker and Koch [56]. Hence, we assume that $\mathbf{K}=[K_{ij}]$ ($i, j = 1, 2$ for 2D problems) is the only correction tensor to determine and that it must be determined based on the comparison between FSI simulation and the SBT model. In the following, we reduce the corrected SBT to the corrected RFT by neglecting interactions between different parts of a flagellum. This is generally an acceptable simplification in the study of micro-swimmers [35] considering the limited accuracy in experimental observation. In RFT, the fluid forces $\mathbf{F}_f$ acting on a slender body is assumed to be proportional to the local velocity of the body. We shall then include **K** in the coefficients of proportionality to establish the CRFT.

For shorthand, we recast equation (3) as:

$$\mathbf{S}(s)=\boldsymbol{\kappa}(s)\cdot\left\{\mathbf{U}(s)+\psi\left[\mathbf{S}(s)\right]\right\}, \tag{4}$$

where $\boldsymbol{\kappa}(s)=[2\mathbf{I}-\hat{\mathbf{x}}(s)\hat{\mathbf{x}}(s)]/[4\ln\kappa(s)]$, and $\psi[\mathbf{S}(s)]$ is the functional of Stokeslets $\mathbf{S}(s)$ and $\psi(\mathbf{0})=\mathbf{0}$. Taking the correction term $\mathbf{K}\cdot\mathbf{S}$ into account, equation (4) is rewritten as:

$$\mathbf{S}(s)=\boldsymbol{\kappa}(s)\cdot\left\{\mathbf{U}(s)+\mathbf{K}\cdot\mathbf{S}(s)+\psi\left[\mathbf{S}(s)\right]\right\}. \tag{5}$$

The approximation of equation (5) can be made based on the scenario of a straight flagellum of a uniform cross-section. In this scenario, **U** and **κ** are constants, and the direction vectors $\hat{\mathbf{x}}$ and $\hat{\mathbf{y}}$ are independent of position s, which greatly simplifies the solution. An iterative procedure can then be adopted. First, the zeroth-order approximation $\mathbf{S}^{(0)}(s)$ can be determined by applying $\mathbf{S}=0$ to the right-hand side of equation (5) and is expressed as:

$$\mathbf{S}^{(0)}(s)=\boldsymbol{\kappa}\cdot\mathbf{U}. \tag{6}$$

Substituting equation (6) into the right-hand side of equation (5) again results in the first-order approximation $\mathbf{S}^{(1)}(s)$. The second-order approximation $\mathbf{S}^{(2)}(s)$ can be obtained similarly and is normally accurate enough for the RFT [35]. Eventually, we can obtain the total fluid force $\mathbf{F}_f$ on a uniform straight flagellum of unit length with a unidirectional motion by substituting $\mathbf{S}^{(2)}(s)$ into equation (2).

Denoted by $U_{\parallel}(s)$ and $U_{\perp}(s)$ the components of $\mathbf{U}(s)$ tangential and normal to the local centerline of a flagellum, respectively, the corresponding fluid forces in the RFT are formulated as:

$$F_{f_{\parallel}}=c_{\parallel}U_{\parallel}, F_{f_{\perp}}=c_{\perp}U_{\perp}. \tag{7a,b}$$

Based on the second-order approximation $\mathbf{S}^{(2)}(s)$ and equation (2), the two coefficients of resistive forces in equation (7*a, b*) in the CRFT can be derived (cf appendix A) as:

$$c_{\parallel}=2\pi\mu\left[\frac{1}{\ln(1/\kappa)}+\frac{\frac{3}{2}-\ln 2-\frac{K}{4}}{\ln^{2}(1/\kappa)}\right.$$
$$\left.+\frac{\left(\frac{3}{2}-\ln 2-\frac{K}{4}\right)^{2}+1-\frac{\pi^{2}}{12}}{\ln^{3}(1/\kappa)}\right], \tag{8}$$

and

$$c_{\perp}=4\pi\mu\left[\frac{1}{\ln(1/\kappa)}+\frac{\frac{1}{2}-\ln 2+\frac{K}{2}}{\ln^{2}(1/\kappa)}\right.$$
$$\left.+\frac{\left(\frac{1}{2}-\ln 2+\frac{K}{2}\right)^{2}+1-\frac{\pi^{2}}{12}}{\ln^{3}(1/\kappa)}\right], \tag{9}$$

where the correction factor $K=K_{11}=-K_{22}$ due to the property of zero divergence of the tensor **K**. Note that when $K=0$, equations (8) and (9) reduce to the RFT expressions in [35]. The proposed CRFT is then applicable to formulate the governing equations of an AFMS based on the bar-joint model.

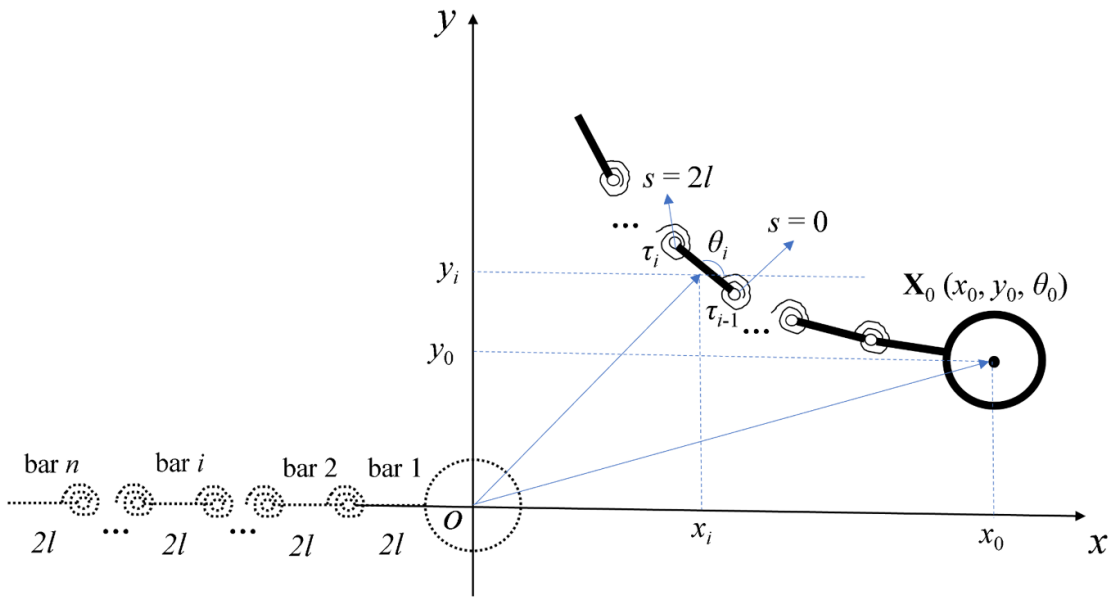

Figure 2. The schematic of the bar-joint model of the AFMS, where the global coordinate system is established with the origin at the centroid of the head and the x- and y-axes being the longitudinal and transverse axes of the flagellum at the initial state, respectively.

2.2. The bar-joint model

Figure 2 demonstrates the bar-joint model of the AFMS. The flagellum is simplified into rigid bars with a constant length 2 l. They are indexed (denoted by i) from 1 to n and connected with linear torsion springs [47]. The ith spring joint connects the bars i and $(i+1)$ and the first $(i=1)$ bar is assumed to be rigidly connected to the head. The motion of the ith bar and the head $(i=0)$ can be represented by the vector of time-dependent variables $\mathbf{X}_i(t) = (x_i, y_i, \theta_i)^{\mathrm{T}}$, where x_i and y_i are coordinates of the midpoint of the ith bar (or the center of the head), and θ_i the angle of rotation with respect to the x-axis (anticlockwise rotation is taken as positive). Correspondingly, the velocity vector of the head $(i=0)$ and bars $(i>0)$ can be represented by $\dot{\mathbf{X}}_i = \left(\dot{x}_i, \dot{y}_i, \dot{\theta}_i\right)^{\mathrm{T}}$, where the overhead dot denotes time derivative.

Based on the CRFT, one can easily obtain the three equilibrium equations of external forces for the bar-joint model, given by:

$$\begin{bmatrix} \mathbf{A}_0 & \mathbf{A} \end{bmatrix} \begin{bmatrix} \dot{\mathbf{X}}_0 \\ \dot{\mathbf{X}} \end{bmatrix} + \mathbf{F}_0 = \mathbf{0}, \tag{10}$$

where $\mathbf{A_0}$ and $\mathbf{A}$ are the resistive matrices of the head and bars (detailed expressions can be seen in equations (B16) and (B19) in appendix B), and $\mathbf{F}_0 = [\mathrm{F}_{extx}, \mathrm{F}_{exty}, \tau_{\mathrm{ext}} + x_0 F_{extx} - y_0 F_{extx}]^{\mathrm{T}}$ is the vector of the external actuation, containing horizontal and horizontal forces (arising from the acoustic actuation) and a torque (about the origin, arising from the magnetic power) on the head.

At the ith joint, the velocities determined from the two connected bars should be equal, i.e. $\mathbf{V}_i(2l) = \mathbf{V}_{i+1}(0)$. These constraints ensure the inextensibility conditions of a flexible flagellum [48, 49]. Since the first bar and the head are assumed to be rigidly connected, one can obtain below $(2n+1)$ equations in terms of the constraints:

$$\begin{bmatrix} \mathbf{0} & \mathbf{T}_V \\ -\mathbf{I} & \mathbf{B} \end{bmatrix} \begin{bmatrix} \dot{\mathbf{X}}_0 \\ \dot{\mathbf{X}} \end{bmatrix} = \mathbf{0}, \tag{11}$$

where $\mathbf{I}$ is a 3×3 identity matrix, $\mathbf{T}_V$ the matrix of kinematic constraints of neighboring bars (see equation (B20)), and $\mathbf{B}$ the kinematic constraints between the first bar and the head (see equation (B23)).

The polymeric (viscoelastic) flagellum is described based on the discrete beam theory [50] in which the inherent damping in most polymers is nonnegligible [24]. The material of the microswimmer is considered to be a kind of isotropic polymer described by the Kelvin–Voigt viscoelastic model [59]. The moment induced by the torsion spring at the ith joint M_i is expressed in a forward difference formula as:

$$M_i = E\frac{J_i + J_{i+1}}{2}\frac{\theta_{i+1} - \theta_i}{2l} + \eta\frac{J_i + J_{i+1}}{2}\frac{\dot{\theta}_{i+1} - \dot{\theta}_i}{2l}, \tag{12}$$

where E and η are the Young's modulus and viscosity coefficient, respectively [60–62], and J_i denotes the second moment of area of the ith bar, where an average value of J between two neighboring bars is adopted to indicate the second moment of area at the ith joint in case the flagellum is non-uniform. Then, the moment equilibrium of the structure leads to the below $(n-1)$ equations (cf appendix B):

$$\begin{bmatrix} \mathbf{D}_0 & \mathbf{D} \end{bmatrix} \begin{bmatrix} \dot{\mathbf{X}}_0 \\ \dot{\mathbf{X}} \end{bmatrix} = \mathbf{F}_E, \tag{13}$$

where $\mathbf{D}$ and $\mathbf{D}_0$ are the matrix of moment balance related to the bars and head, respectively, which are expressed in equations (B25) and (B29), and $\mathbf{F}_E$ is a list of torques, which is expressed in equation (B31) in appendix B.

Finally, combining equations (10)–(13), the governing ODEs of the bar-joint model based on the CRFT can be expressed as:

$$\begin{bmatrix} \mathbf{A}_0 & \mathbf{A} \\ \mathbf{0} & \mathbf{T}_V \\ -\mathbf{I} & \mathbf{B} \\ \mathbf{D}_0 & \mathbf{D} \end{bmatrix} \begin{bmatrix} \dot{\mathbf{X}}_0 \\ \dot{\mathbf{X}} \end{bmatrix} = \begin{bmatrix} -\mathbf{F}_0 \\ \mathbf{0} \\ \mathbf{0} \\ \mathbf{F}_E \end{bmatrix}. \tag{14}$$

The nondimensionalization of equation (14) can be taken by choosing the half-length of a bar l, the period of the acoustic actuation $T = 1/f_r$, and the fluid viscosity μ as the reference variables based on the Buckingham π theorem [63]. The dimensionless quantities are detailed in appendix B. Equation (14) can be solved by using the built-in ODE solver *ode15s* in MATLAB [64].

3. Results and discussion

3.1. Problem statement and convergence analyses of FSI simulations

We consider an AFMS requiring acoustic excitations to propel. The concerned AFMS is composed of a rigid head and a flexible slender flagellum, as exhibited in figure 3, where the structure has been meshed for the FSI simulation. The AFMS suspends in an aqueous solution and swims under an acoustic actuation that leads to the oscillations of the head and the whipping of the flagellum. According to the study of Liu and Ruan [24], the effect of periodic acoustic excitation for an AFMS can be assumed to be a periodic force F_{ext} acting on the head with the actuation frequency f_r, that is $F_{\text{ext}}(t) = F_a \cos\omega t$, where $\omega = 2\pi f_{\text{r}}$ is the angular frequency and F_a is the amplitude. The head oscillation induced by F_{ext} whips the flagellum, giving rise to the advancement of the AFMS at an average speed of V_{ave}. We focus firstly on the swimming problem that the average displacement of the micro-swimmer during several actuation periods keeps a straight line. It has been demonstrated both experimentally [14, 65] and theoretically [24, 40, 47] that the micro-swimmer tends to align itself perpendicular to the direction of F_{ext}. Hence, in the following FSI simulations, the only boundary condition is that the centroid of the head (or the end of the flagellum if the micro-swimmer has no head) is subject to a transverse harmonic force F_{ext}. Consequently, the head oscillates transversely with an amplitude A_{amp}.

Figure 3 shows the mesh of the FSI model that was simulated using a built-in fully coupled 2D FSI solver in COMSOL Multiphysics [66]. The whole geometry can be divided into two domains: a rectangular fluid domain of 2000 × 500 μm^2 (capacious enough for a micro-swimmer) and a solid one for the AFMS in the center of the fluid. The radius of the circular head and the length of the flagellum are denoted by R_H and L, respectively. For a 2D simulation, the cross-section of the flagellum is rectangular. The flagellar width W_y can be either uniform or tapered with a maximum of W_{y0} at the root (the joint between the head and the flagellum). The micro-swimmer is assumed to have a uniform thickness of W_z.

We investigate the steady-state swimming performances using the trajectory of the center of the head (or the right end of the flagellum). In the numerical simulations, the incompressible creeping flow module without the inertial term (Stokes flow) is employed for the fluid domain, while the solid mechanics module with plane strain approximation for the solid domain [67]. The micro-swimmer consists of two material models: a viscoelastic material for the flagellum and a rigid domain for the head [59]. Considering the expected medical applications and the current experiments, the flagellar material is assumed to be a Kelvin–Voigt viscoelastic material for representing an organic polymer, such as the polypyrrole employed in [13] and the polyethylene glycol employed in [14]. F_{ext} is applied along the y-direction to the centroid of the head. If headless, F_{ext} is applied to the right end of the flagellum. The automatic remeshing technique is employed to tackle the problems induced by large rigid-body motions, where the fluid domain (i.e. the gray area in figure 3) is set as the moving mesh region based on the Winslow smoothing method [68], in which the mesh distortion parameter is set to unity.

We first exemplify 2D simulations of two AFMS models as shown in figures 4(a) and (b). The first (figure 4(a)) one is a uniform flagellum (without head) with dimensions: $L = 200$ μm, $W_z = 40$ μm, and $W_y = 12$ μm, and swims in a fluid with the dynamic viscosity: $\mu = 0.1$ Pa·s. The second one (figure 4(b)) is a sperm-like micro-swimmer referring to the AFMS described in [14]. It has a thickness, $W_z = 20$ μm, and a cylindrical head with a radius: $R_H = 20$ μm, and a tapered flagellum: $L = 200$ μm and $W_y = W_{y0}(1 - \lambda X)$, where $0 \leqslant X \leqslant 1$ is the length normalized by L, $W_{y0} = 20$ μm, and the tapering index $\lambda = 0.9$. Both micro-swimmers have the material properties: $E = 10$ MPa and $\eta = 10$ Pa·s and in the static fluids ($\mathbf{u} = 0$).

Figures 4(a) and (b) illustrate the fluid pressure distribution at $t = 0.005$ s. An vertical acoustic force F_{ext} was applied at the right with a frequency of $f_r = 1000$ Hz and an amplitude of 2.7 μN and 4 μN, for the uniform flagellum (figure 4(a)) and the sperm-like micro-swimmer (figure 4(b)), respectively, to maintain an amplitude

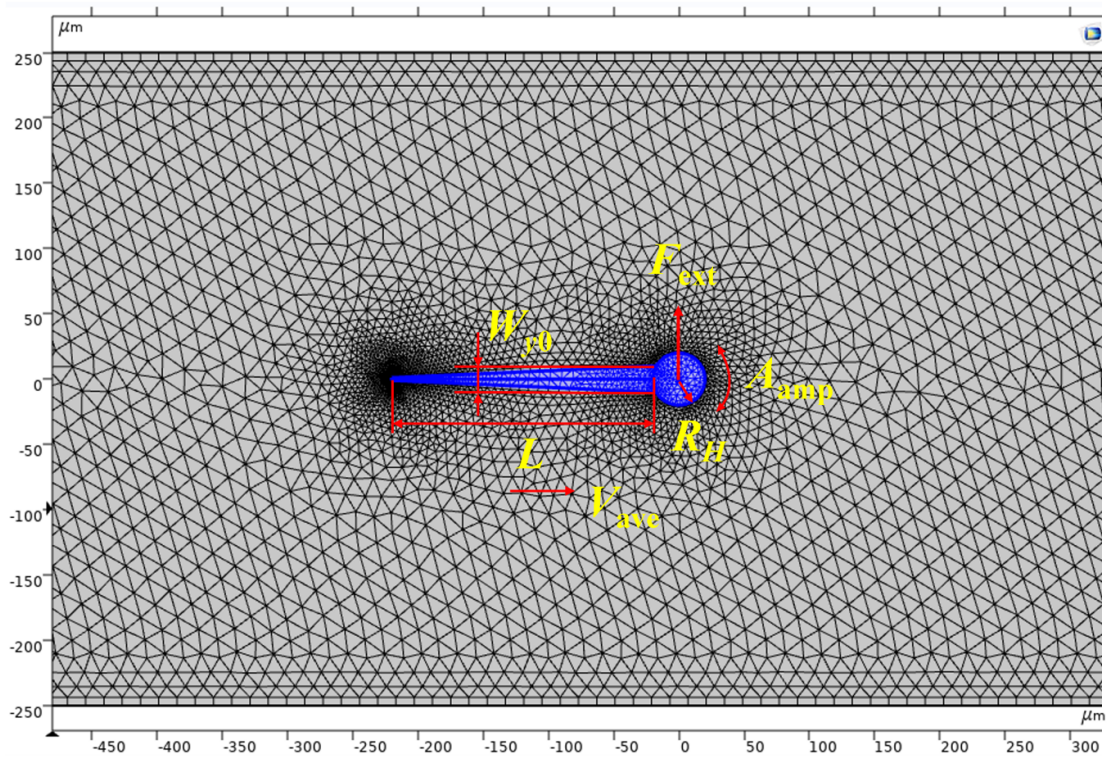

Figure 3. The configuration of a FSI simulation, wherein the gray area represents a mesh result of the fluid, and the blue area illustrates the deformable AFMS domain.

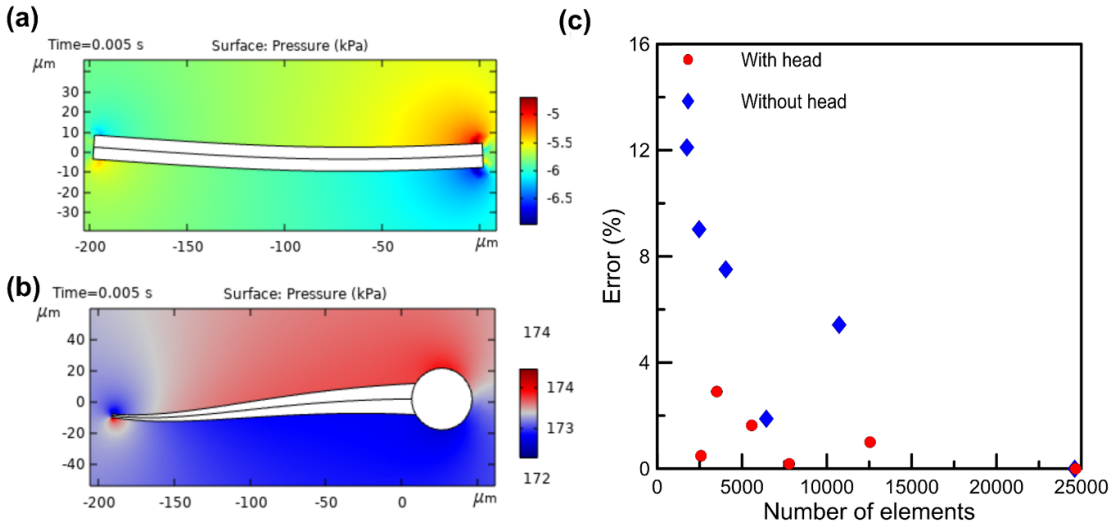

Figure 4. Examples of convergence analyses of the FSI simulation with common parameters $L = 200$ μm, $E = 10$ MPa, $\eta = 10$ Pa s, $\mu = 0.1$ Pa·s, $A_{amp} = 20$ μm, and $f_r = 1000$ Hz: (a) the pressure distribution of a uniform flagellum without head at the end of the fifth actuation period ($t = 0.005$ s) with $R_H = 0$, $\lambda = 0$, $W_{y0} = 12$ μm, $W_z = 40$ μm, and $F_a = 2.7$ μN; (b) the pressure distribution of a tapered flagellum with head at the end of the fifth actuation period ($t = 0.005$ s) with $R_H = 20$ μm, $\lambda = 0.9$, $W_{y0} = 20$ μm, $W_z = 20$ μm, and $F_a = 4$ μN; (c) convergence analyses in terms of the number of elements for the cases with (red solid line) and without (blue dotted line) head.

of $A_{amp} = 20$ μm at the actuated end. It is observed that the average trajectory within a period of acoustic excitation is nearly a straight line parallel to the x-axis. The average (over one period) velocity in the first two periods varies (transient motion) and afterwards stabilizes at 383.4 μm·s^{-1} (figure 4(a)) or 5537 μm·s^{-1} (figure 4(b)). For the micro-swimmer herein, considering the fluid density $\rho \sim 10^3$ kg·m^{-3}, which leads to the Reynolds number $\mathrm{Re} = \rho LV/\mu = 7.668 \times 10^{-4}$, which is sufficiently small to warrant the employment of the RFT. The stabilized terminal velocity V_{ave} is obtained with the simulation domain having

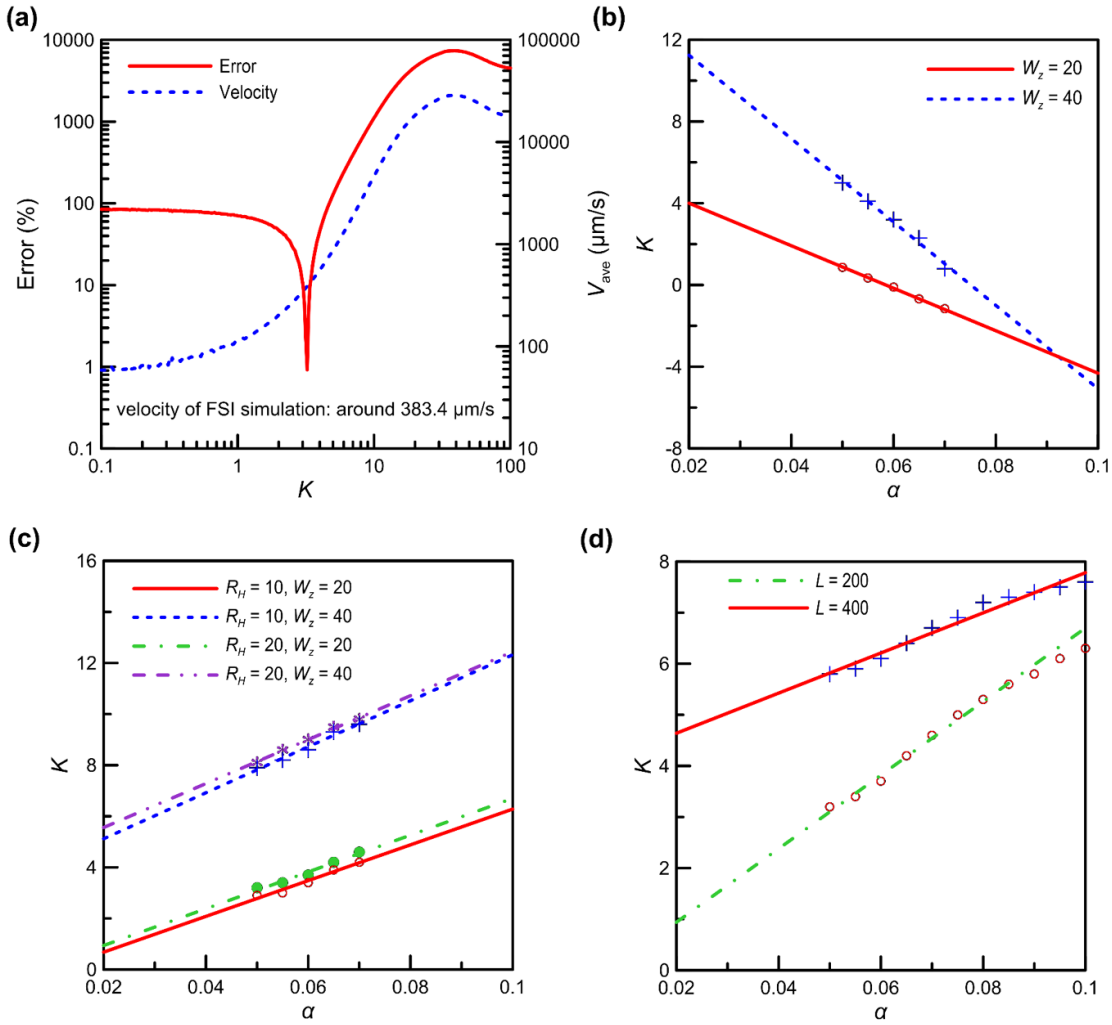

Figure 5. Estimate of K for uniform flagella with parameters $\eta = 10$ Pa·s, $\mu = 0.1$ Pa·s, and $A_{amp} = 20$ μm (other paramours are provided in table 1): (a) example of the error (red solid line) V_{ave} obtained from the CRFT model (blue dashed line) based on the simulation result ($V_{ave} = 383.4$ μm·s^{-1}) when K varies; (b) relations between K and α for a flagellum without head; (c) relations between K and α for an AFMS with head; (d) relations between K and α for AFMSs with different flagellum length.

around 10^4 elements (figure 4(a)) or 2×10^4 elements (figure 4(b)). Figure 4(c) illustrates the relative errors for the cases without and with head, respectively, in terms of the number of elements used in the FSI simulations. It is noted that the simulation results have converged (i.e. the deviation is within 5%) when the number of elements is more than 10^4, indicating that the FSI simulation is convergent and stable.

3.2. Determination of K

The correction factor K is determined by comparing the terminal average velocities V_{ave} obtained from the FSI simulations and the CRFT-based bar-joint model (the convergence analysis of the bar-joint model can be seen in appendix C). As an example, figure 5(a) shows the results of CRFT-based bar-joint model when K sweeps from 0.1 to 100 for the case of a uniform flagellum without head. In solving the bar-joint model, we also set $A_{amp} = 20$ μm to determine V_{ave} (blue dotted curve in figure 5(a)), and the deviations (red curve in figure 5(a)) from the simulation result (383.4 μm·s^{-1}) has a sharp minimum at $K = 3.2$, which is less than 1%.

In principle, adjusting K can lead to an excellent agreement between simulation and CRFT results. In the following estimate of K for different cases, we set the criterion of acceptable deviation in V_{ave} to be 5% to balance the computational efficiency and accuracy and demonstrate several relations between K and the flagellum slenderness α ($\alpha = W_y/L$) in figures 5(b)–(d). In order to ensure that the flagellum is still a slender body, we set α in the range of 0.05–0.07 [31]. Figures 5(b) and (c) show that K varies almost linearly with α, and the slope depends on the thickness W_z, for both the uniform flagellum without a head and the sperm-like micro-swimmer with a rigid-cylindrical head, respectively. The detailed expressions of K in terms of α obtained through linear regression are listed in table 1.

In table 1, one can note that the existence of a head can change the slope of the linear K–α relation from a negative value to a positive one. Besides, as

Table 1. The fitting expressions of K in terms of α, λ or β under different combinations of geometric parameters.

L (μm)	R_H (μm)	W_z (μm)	W_{y0} (μm)	λ	f_r (Hz)	E (MPa)	M (μm)	Expression of K	Figures
200	0	20	10–14	0	1000	10	0.1	$K=-104\alpha+6.08$	4(b)
200	0	40	10–14	0	1000	10	0.1	$K=-204\alpha+15.32$	4(b)
200	10	20	10–14	0	1000	10	0.1	$K=7\alpha-0.72$	4(c)
200	10	40	10–14	0	1000	10	0.1	$K=90\alpha+3.32$	4(c)
200	20	20	10–14	0	1000	10	0.1	$K=72\alpha-0.5$	4(c)
200	20	40	10–14	0	1000	10	0.1	$K=86\alpha+3.84$	4(c)
400	20	20	20–40	0	1000	10	0.1	$K=39.27\alpha+3.854$	4(d)
200	20	20	20	0.1–0.9	1000	10	0.1	$K=-1.29\lambda+6.43$	5(a)
200	20	20	20	0.9	500–7000	10	0.1	$K=(0.036\beta^2+2.40\beta+24.5)/(\beta+0.12)$	5(b)
200	20	20	20	0.9	1000	3–70	0.1	$K=(0.087\beta^2-2.07\beta+106)/(\beta+7.78)$	5(b)
200	20	20	20	0.9	1000	10	0.05–0.7	$K=(0.016\beta^2+1.40\beta+41.4)/(\beta+0.89)$	5(b)

observed in figure 5(c), the variation of R_H can hardly influence the K–α curve. In addition, K doubles when the depth W_z increases from 20 to 40 μm, as shown in figures 5(b) and (c), and also doubles when L increases from 200 to 400 μm, as shown in figure 5(d). These results suggest that, roughly speaking, K is linearly dependent on the volume of the flagellum. In figure 5(d), α is sampled from 0.05 to 0.1, and the fitting equation obtained in the α range of 0.05–0.07 is used. In the 0.07–0.1 range, the difference between the fitting equation and the actual results of K are still below 3%.

When a tapered flagellum is discretized into be a bar-joint model, these bars have uniform dimensions. In this case, the fitting equations of K for a uniform flagellum may be directly employed. For example, consider the micro-swimmer with $L = 200$ μm and $R_H = W_z = W_{y0} = 20$ μm, assume that the width of the ith bar, i.e. W_{yi}, follows the tapering equation (equation (C1)) and that the slenderness of the ith bar, i.e. α_i, equals W_{yi}/L, the correction factor of the ith bar, i.e. K_i, can then be estimated according to the fitting curve of K in figure 5(d). In this way we can directly obtain the terminal average velocity V_{ave} based on the CRFT model without implementing the FSI simulation. We herein designate this method as the direct-K method. Straightforward though this method is, its outcomes can deviate from those of the FSI simulation, and the corresponding error in terms of the tapering index λ is illustrated in blue dotted line in figure 6(a). For the classical RFT model, i.e. $K_i = 0$ for each bar, the error exceeds 90%. For the direct-K method, it is noted that the error is around 12% for $\lambda > 0.2$, which indicates that if we directly apply the fitting expression of K arising from the case of a uniform flagellum to the case of a tapered one, the error can decrease by about 80% from the results of RFT. However, the deviation is still considerable.

More accurate results for a tapered flagellum can be achieved by assuming all bars having identical K, i.e. $K_i = K$. In this way, we treat a tapered flagellum to be an equivalent uniform one with an effective K, and thus this method is regarded as the effective-K method. The red circles in figure 6(a) represent the effective K at different λ, and the red solid line is the corresponding linear fitting: $K = -1.29\lambda + 6.43$. It is noted that in figure 6(a) for $\lambda \leqslant 0.1$, magnitude of the effective K is nearly identical to that of the case of $\lambda = 0$, and the error of the effective-K method is close to 0, indicating that the effect of tapering on hydrodynamics only works when $\lambda > 0.1$.

Note that the above results of K are obtained with the specific material and actuation parameters. We find that A_{amp} and η hardly affect the determination of K, while f_r, E and μ can have considerable influence. For example, for the micro-swimmer as shown in figure 4(b) in section 3.1, we varied f_r, E and μ to check their influence on K. It is noted that the combined term $\beta = \mu f_r/E$ is an important non-dimensional parameter in the governing equations of flagellum's hydrodynamics. For example, β enters into the elastohydrodynamic penetration length [40]: $\sqrt[4]{(EJ)/(2\pi c_\perp f_r)}$, proportional to $\sqrt[4]{1/\beta}$, and the sperm number [69]: $L\sqrt[4]{(2\pi c_\perp f_r)/(EJ)}$, proportional to $\sqrt[4]{\beta}$. Hence, we plot the relations between K and β in figure 6(b) with the corresponding fitting equations listed in table 1. It is noted that when β is between 5 and 20, the variations of K in terms of f_r, E and μ collapse to the same curve. When $\beta > 20$, the effects of E and μ are still the same and tends to level off; nevertheless, the effect of head excitation frequency f_r tends to lean upwards. The difference in K increases with the increase in f_r and μ (or decrease in E) when $\beta > 20$ because raising f_r can considerably enhance V_{ave} (which leads to a larger K) as it can induce the change of the flagellum's wiggling profile (e.g. bringing about smaller wavelength). Instead, increasing μ or reducing E only leads to larger resistive forces under the same wiggling profile, which results in a small enhancement in V_{ave}.

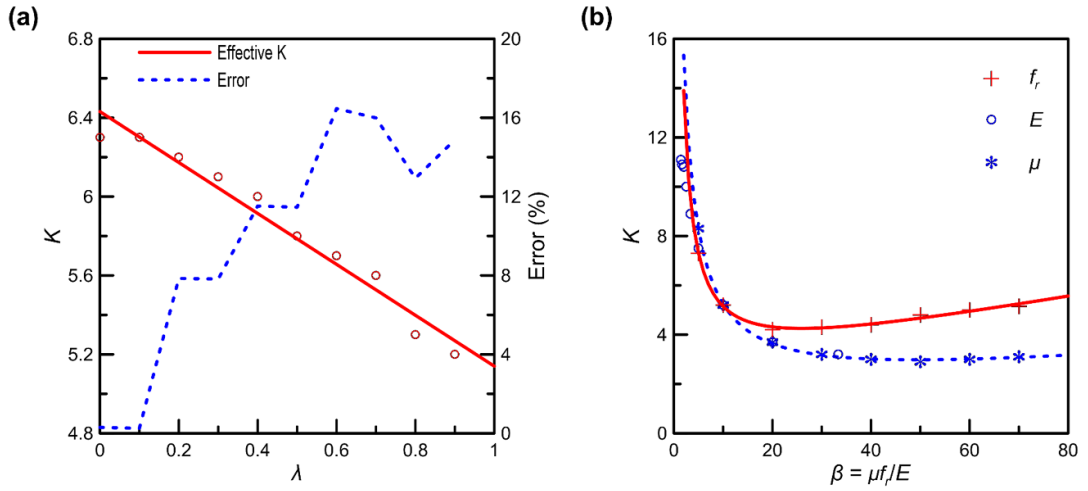

Figure 6. Estimate of K for tapered flagella with parameters $\eta = 10$ Pa·s, $\mu = 0.1$ Pa·s, and $A_{amp} = 20$ μm (other paramours are provided in table 1): (a) relations between K and λ and between the error and λ, respectively, where the fitting curve of K (red solid line) is obtained by the effective-K method, and the error of V_{ave} (blue dotted line) is obtained by the direct-K method; (b) the relation between K and β obtained by varying f_r (red cross), E (blue circle), or μ (blue star), respectively.

3.3. Examples of verification

In order to explicate the validity of the method for correcting RFT, we compare three head trajectories (or the trajectories of the right end of the flagellum for the case without head) calculated by FSI simulations and by CRFT. Figure 7 exhibits the trajectories and their errors from FSI simulations and the CRFT models for the acoustic-actuation period from 20 to 25. The corresponding geometries of AFMSs at four instances which equally divide the last period in the FSI simulation (outline) and the CRFT model (centerline) are given as the insets. The supplementary videos of the corresponding FSI simulations and relevant codes of the CRFT model for verification are provided in the supplementary documents.

Figures 7(a), (c) and (e) show the trajectories of FSI simulations and CRFT models for the case of a uniform flagellum without a head, a uniform flagellum with a head, and a tapered flagellum with a head, respectively. To approximate the trajectories based on the CRFT model, the corresponding K are determined to be 3.2, 6.3, and 5.2, respectively, based on the fitting equations suggested in the last section. It is noted that each of the trajectories obtained based on the CRFT model has an offset from the FSI-simulated one, reflecting the slight difference in the propulsive forces. This is due to the determination of K, in which we allowed a 5% tolerance in the motility difference. The distance between the positions of the AFMS head obtained from the FSI simulation and those from the CRFT solution, after dividing by the flagellum length L, is defined as the position error of CRFT solution, which are shown in figures 7(b), (d) and (f) (from 20 to 25 periods) and their insets (for first 40 periods). One may note that in figures 7(b) and (f), there are some small spikes, whereas in figure 7(d) the errors are simply oscillating. Several extreme error points in figures 7(b), (d) and (f) are indicated in figures 7(a), (c) and (e), respectively, where the corresponding differences between the two solutions are indicated by dashed lines. It is noted that the spikes of errors are due to the oscillatory motions, resembling the interference of waves.

The insets in figures 7(b), (d), and (f) show that the position errors in 40 periods are well below 4%. Because of the small motility difference (i.e. the tolerance in determining K), the trajectory deviations are caused; nevertheless, these deviations are well bounded and remain small when normalized by the length of the flagellum. Such small errors indicate that the CRFT-based bar-joint model, as described in section 3, renders an excellent approximation to numerical simulations. It should be noted that such position errors can be further reduced if we set a more stringent requirement in accuracy in determining K.

3.4. An application of the CRFT-based bar-joint model

We expect that the proposed CRFT-based bar-joint model can ultimately be employed for the path planning and navigation control of AFMSs because of the excellent agreement between the FSI and the simplified model has been revealed. Here, as the final demonstration, we employ CRFT to study the turning strategy for an AFMS, which is essential and inevitable in practical applications. It is noted that FSI simulation for turning is unconverted in our trials due to excessively distorted elements; hence, we only provide the results of CRFT model.

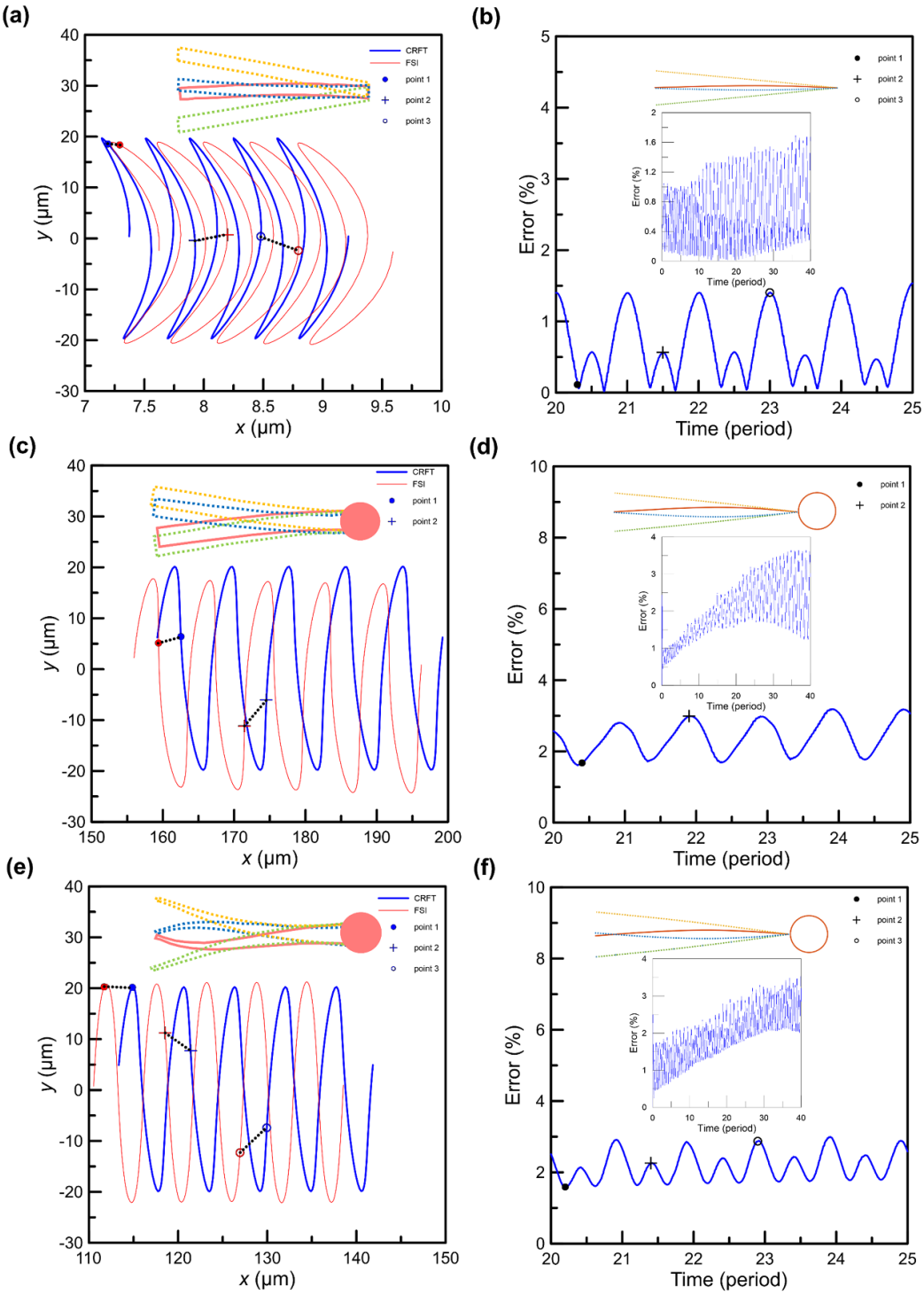

Figure 7. Verifications of the CRFT model: the head trajectories obtained from the FSI simulations (red lines) and CRFT-based bar-joint models (blue lines) for the cases of (a) a uniform flagellum without head, (c) a uniform flagellum with head, and (e) a tapered flagellum with head, and (b) and (d) and (f) the corresponding trajectory errors which are the distances between two head positions at the same time scaled by the length of the flagellum, respectively. The marked points in (b) and (d) and (f) indicate that the trajectory errors reach their extreme values, where the corresponding distances between the pairs of trajectory points are indicated by the dashed lines in (a) and (c) and (e). To have a clearer comparison, only the periods from 20 to 25 are shown. The insets in (b) and (d) and (f) show the trajectory errors for a long time (40 periods).

In the following demonstration, the AFMS is identical to the one shown in figure 7(e). We expect that the external force $\mathbf{F}_{\text{ext}}$ ($\mathbf{F}_{\text{ext}} = [F_{\text{extx}}, F_{\text{exty}}]^{\text{T}}$) can be applied to the head of an AFMS through applying acoustic waves. According to [24], under an acoustic planewave rendering a 2D fluid displacement field $\mathbf{A}_{\text{acou}}$ with the amplitude A_{acou}, the oscillation amplitude of the head ($R_H = 20$ μm) of the AFMS A_{amp} is approximately $1.67A_{\text{acou}}$ if the sound wavelength is far greater than the dimensions of the head. In this case, the oscillatory velocity in the fluid is nonzero, i.e. $\mathbf{u} = \partial\mathbf{A}_{\text{acou}}/\partial t$.

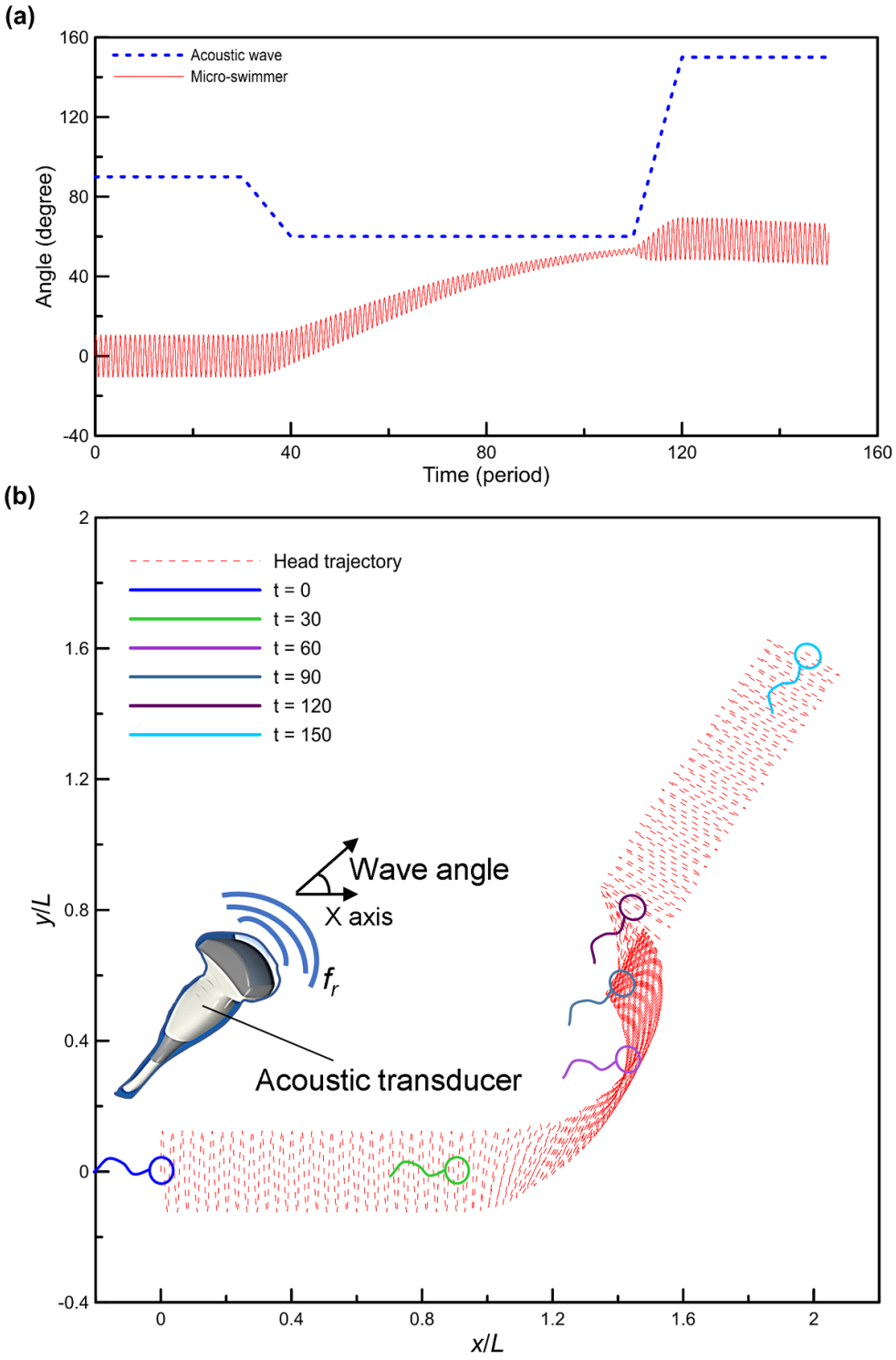

Figure 8. Application of the CRFT model where the AFMS is steered by acoustic waves: (a) the rotation angle with respect to the *x*-axis in terms of actuation period for the acoustic waves (blue dashed line) and the AFMS (red solid line); (b) the trajectory and orientations of the AFMS within 150 periods; the insets sketch the acoustic steering strategy, and the time *t* is in terms of the number of acoustic periods.

One may note from the trajectories in figure 7 that an AFMS tends to move along the direction perpendicular to $\mathbf{F}_{ext}$ that induces head oscillations, which is also the case in the experiments of acoustic actuation [65]. Hence, steering an acoustically propelled AFMS might be achieved by rotating $\mathbf{F}_{ext}$ and we can design such a turning method using only acoustic power based on the CRFT model. Considering an acoustic planewave that can gradually change the direction of propagation, hence changing the direction of $\mathbf{F}_{ext}$ on the head of an AFMS. As shown in figure 8(a), we let the angle of the acoustic

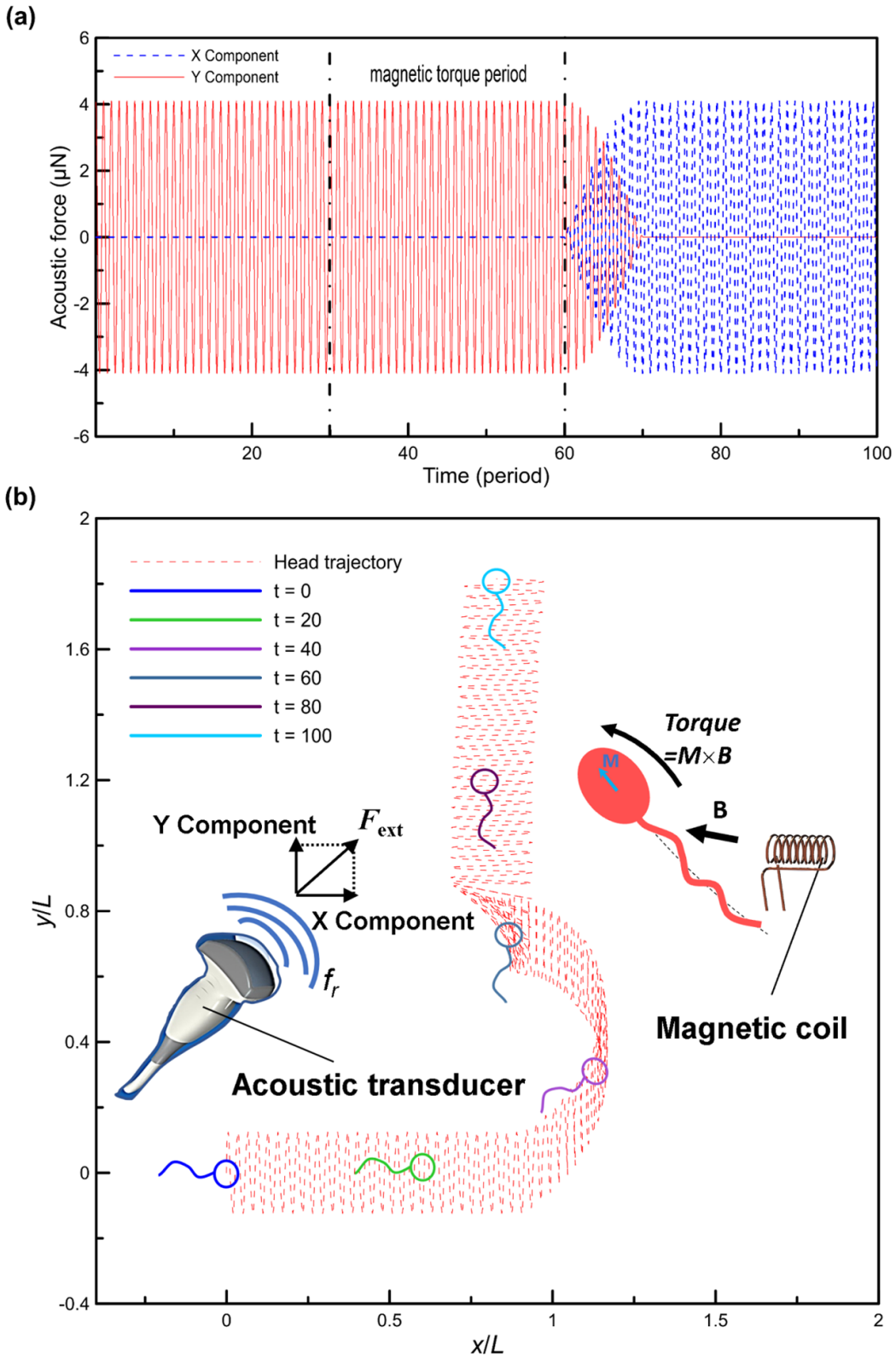

Figure 9. Application of the CRFT model where the AFMS is steered by a magneto-acoustic strategy: (a) the applied acoustic forces for propulsion in terms of actuation period along x (blue dashed line) and y (red solid line) directions (Note: the actuation forces along y (x) direction linearly decreases (increases) between the 60th period and the 70th period to assist turning), and from the 30th and 60th periods, a magnetic torque is applied; (b) the trajectory and orientations of the AFMS within 100 periods; the insets sketch the remote magneto-acoustic steering strategy.

wavevector rotates from 90° to 60° (counterclockwise from positive direction of x-axis) in 10 periods. After the change, the angle of the micro-swimmer is around 5°. Maintaining $\mathbf{F}_{ext}$ at 60° for 100 periods, the angle of the AFMS gradually drift to be close to 60°. Further turning $\mathbf{F}_{ext}$ to 150° in 10 periods leads the angle

of the micro-swimmer to move along the straight line of 60°. The detailed trajectory of the AFMS is shown in figure 8(b).

The above example shows that using only acoustic power to control AFMSs is possible in theory, although the orientation relation between an AFMS and acoustic wavevector is nontrivial, depending on the parameters of the actuation and the swimmer [70]. If the direction of wavevectors can be accurately adjusted, these waves can induce head oscillation and flagellum wiggling for propulsion and steering. In these attempts, our AFMS model can provide the formalism for the trajectory prediction and manipulation, which will lay the foundation for controlling micro-swimmers to carry out precision therapies for cancers and other diseases requiring non-invasive and localized treatments.

If a torque can be applied to the head of an AFMS, turning will be easier and more controllable. This can be achieved by introducing magnetic particles (MPs) into the head [71], resulting in a magnetized head along an easy axis (**M**), and applying an external magnetic field (**B**) unparallel with the head's easy axis, resulting in a torque $\boldsymbol{\tau}_{\text{ext}} = \mathbf{M} \times \mathbf{B}$ on the head, as sketched in the inset in figure 9(b). Note that the acoustic power is still used for propulsion but not for steering. The external magnetic field used in hyperthermia-based therapy is usually around 10 mT [72] and that the volumetric magnetic susceptibility is in the order of 10^5 for ferromagnetic MPs [73], accordingly, the magnetic-induced torque by single MP of 1 μm is around 4×10^{-12} N·m. With five MPs in the head, the total magnetic torque on the head is 2×10^{-11} N·m, which is assumed in the following calculation. For such a magneto-acoustic method, we design the variations of F_{extx}, F_{exty} and τ_{ext} as shown in figure 9(a), which results in the trajectory of the AFMS as shown in figure 9(b). Hence, the proposed magneto-acoustic maneuver is feasible based on the existing technologies and our theoretical analysis of magneto-acoustic steering can be employed for targeted therapies which require the accurate and rapid navigation.

4. Conclusions

In this work, we have described a CRFT and the CRFT-based 2D bar-joint model for modeling AFMSs propelled by acoustic actuation. The main purpose of this work is to allow a simplified AFMS model to be correctable, verifiable, and in future, applicable for practical applications. The CRFT is inspired by the derivation of the SBT for non-circular flagellum and only introduced is the single correction factor K. However, K depends on not only geometrical parameters but also other factors influencing a flagellum's wiggling profiles, such as material properties and actuation frequency. Hence, although the CRFT is derived from the non-circular SBT, K should be determined after some knowledge of the motility of an AFMS are obtained. In the exercises, we determined K by comparing the terminal average velocities obtained from the CRFT-based bar-joint models propelled by acoustic waves and those from the FSI simulations. After correction, it is shown that the difference in the detailed trajectory can be well below 4%. In our work, K is very weakly dependent on the head radius R_H and linearly dependent on the slenderness α and the tapering factor λ. Hence, it is not difficult to determine these dependences and then employ CRFT to optimize the geometry of an AFMS for maximizing the motility. With CRFT, the controlled navigation of AFMSs can also have a high-level robustness. For this point, we have demonstrated the possible strategies of turning an AFMS using acoustic or magneto-acoustic fields, which indicates that the current CRFT model includes enough information to deal with a turning activity.

Before closing this work, the insufficiency of the current CRFT model must be remarked. The current empirical method for the determination of K is tedious and ungeneralizable to the scenarios beyond the parametric space studied in this work, as it requires FSI simulations. An analytical expression of K as a function of geometric, materials, and actuation parameters of an AFMS (i.e. without simulation) is desired, which will be our effort in the future work. In addition, the effectiveness of the CRFT model has not been examined in experiments. It is necessary to fabricate AFMS embedded with magnetic nanoparticles to determine the motility and magneto-acoustics turning performance to verify our model. As the final remark, we stress that this work only analyzed the propulsion caused by oscillations of the head of a microswimmer. The effect of acoustic streaming on the tip of a flagellum, as discussed in [13, 74], was not analyzed. Such a tip force field may also induce the wiggling of a flagellum. In our model, it may also be simplified to be the external force, $\mathbf{F}_0$, acting on the tip. The detailed expression of such tip-induced propulsion is worth exploring in future work.

Data availability statement

All data that support the findings of this study are included within the article (and any supplementary files).

Acknowledgments

This work was supported mainly by NSFC/RGC Joint Research Scheme (Project No. N_PolyU519/19) and partially by the project of International Cooperation and Exchanges of NSFC (No. 51961160729). The authors are grateful for the financial support.

Appendix A. Detailed derivation of the CRFT

When a slender body with uniform cross-section remains straight in motion, $\mathbf{U}$ and $\boldsymbol{\kappa}$ become constants and the direction vectors $\hat{\mathbf{x}}$ and $\hat{\mathbf{y}}$ are independent of position s, i.e. $\mathbf{P}(s) = s\hat{\mathbf{x}}$, and $\mathbf{P}_{s\delta} = -\delta\hat{\mathbf{x}}$. Hence, equation (5) can be simplified as:

$$\begin{aligned}\mathbf{S}(s) = &\frac{2\mathbf{I}-\hat{\mathbf{x}}\hat{\mathbf{x}}}{4\ln\kappa}\cdot\left\{\mathbf{U}+\mathbf{K}\cdot\mathbf{S}(s)+S_{\perp}(s)\hat{\mathbf{y}}\right.\\ &+\ln\left[4s(1-s)\right]\mathbf{S}(s)+S_{\parallel}(s)\left\{\ln\left[4s(1-s)\right]-2\right\}\hat{\mathbf{x}}\\ &\left.+\int_{-s}^{1-s}\left[(\mathbf{I}+\hat{\mathbf{x}}\hat{\mathbf{x}})\cdot\frac{\mathbf{S}(s+\delta)-\mathbf{S}(s)}{|\delta|}\right]\mathrm{d}\delta\right\}. \quad \text{(A1)}\end{aligned}$$

When the body moves tangentially to its centerline, resulting in the Stokeslet vector $\mathbf{S}(s) = S_{\parallel}(s)\hat{\mathbf{x}}$, and the relative velocity $\mathbf{U} = U_{\parallel}\hat{\mathbf{x}}$, then equation (A1) is recast as:

$$\begin{aligned}S_{\parallel}(s) = &\frac{1}{2\ln\kappa}\left\{\frac{U_{\parallel}}{2}+S_{\parallel}(s)\left[\frac{K_{11}}{2}+\ln\left(4s-4s^2\right)-1\right]\right.\\ &\left.+\int_{-s}^{1-s}\frac{S_{\parallel}(s+\delta)-S_{\parallel}(s)}{|\delta|}\mathrm{d}\delta\right\}. \quad \text{(A2)}\end{aligned}$$

The zeroth iterative of equation (A2) is expressed as:

$$S_{\parallel}^{(0)}(s) = \frac{U_{\parallel}}{4\ln\kappa}. \quad \text{(A3)}$$

Replacing $S_{\parallel}(s)$ on the right side of equation (A2) with the right-hand side of equation (A3) reaches the first iterative of the tangential Stokeslet, expressed as:

$$S_{\parallel}^{(1)}(s) = \frac{U_{\parallel}}{4\ln\kappa}\left\{1+\frac{1}{2\ln\kappa}\left[\frac{K_{11}}{2}+\ln\left(4s-4s^2\right)-1\right]\right\}. \quad \text{(A4)}$$

Replacing $S_{\parallel}(s)$ on the right side of equation (A2) with the right-hand side of equation (A4) reaches the second iterative of the tangential Stokeslet, expressed as:

$$\begin{aligned}&S_{\parallel}^{(2)}(s)\\ &= \frac{U_{\parallel}}{4\ln\kappa}\left\{1+\frac{K_{11}}{4\ln\kappa}+\left(\frac{K_{11}}{4\ln\kappa}\right)^2+\left(\frac{1}{2\ln\kappa}+\frac{K_{11}}{4\ln^2\kappa}\right)\right.\\ &\quad\times\left[\ln\left(4s-4s^2\right)-1\right]+\left[\frac{\ln\left(4s-4s^2\right)-1}{2\ln\kappa}\right]^2\\ &\quad\left.+\int_{-s}^{1-s}\frac{\ln\left[4(s+\delta)(1-s-\delta\quad)\right]-\ln\left(4s-4s^2\right)}{(2\ln\kappa)^2}\frac{\mathrm{d}\delta}{|\delta|}\right\}. \quad \text{(A5)}\end{aligned}$$

Then the total tangential fluid force of the slender body of unit length can be obtained based on equation (2) and is expressed as:

$$\begin{aligned}F_{f\parallel} &= -8\pi\mu\int_0^1 S_{\parallel}^{(2)}(s)\,\mathrm{d}s\\ &= -8\pi\mu\frac{U_{\parallel}}{4\ln\kappa}\left\{1+\frac{K_{11}}{4\ln\kappa}+\left(\frac{K_{11}}{4\ln\kappa}\right)^2\right.\\ &\quad+\left(\frac{1}{2\ln\kappa}+\frac{K_{11}}{4\ln^2\kappa}\right)\int_0^1\left[\ln\left(4s-4s^2\right)-1\right]\mathrm{d}s\\ &\quad+\frac{1}{(2\ln\kappa)^2}\int_0^1\left[\ln\left(4s-4s^2\right)-1\right]^2\mathrm{d}s+\frac{1}{(2\ln\kappa)^2}\\ &\quad\left.\times\int_0^1\int_{-s}^{1-s}\frac{\ln\left[4(s+\delta)(1-s-\delta)\right]-\ln\left(4s-4s^2\right)}{|\delta|}\mathrm{d}\delta\mathrm{d}s\right\}\\ &= -2\pi\mu\frac{U_{\parallel}}{\ln\kappa}\left\{1+\frac{K_{11}}{4\ln\kappa}+\left(\frac{K_{11}}{4\ln\kappa}\right)^2+\left(\frac{1}{2\ln\kappa}+\frac{K_{11}}{4\ln^2\kappa}\right)\right.\\ &\quad\times(2\ln 2-3)+\frac{1}{(2\ln\kappa)^2}\left[4\left(\frac{3}{2}-\ln 2\right)^2+4-\frac{\pi^2}{3}\right]\\ &\quad\left.+\frac{1}{(2\ln\kappa)^2}\left(-2.724\times10^{-8}\right)\right\}\\ &= 2\pi\mu U_{\parallel}\left[\frac{1}{\ln(1/\kappa)}+\frac{\frac{3}{2}-\ln 2-\frac{K_{11}}{4}}{\ln^2(1/\kappa)}\right.\\ &\quad\left.+\frac{\left(\frac{3}{2}-\ln 2-\frac{K_{11}}{4}\right)^2+1-\frac{\pi^2}{12}}{\ln^3(1/\kappa)}\right]. \quad \text{(A6)}\end{aligned}$$

The tangential coefficient of resistive force, i.e. equation (8), can be obtained from equation (A6) by setting $K_{11} = K$ (note we have assumed that $K_{22} = -K_{11}$ due to the property of zero divergence of the tensor $\mathbf{K}$). It is found that the influence of δ on the integral is negligible ($\sim10^{-8}$), which justifies RFT. To compare this expression with the classical one, we can construct the identical equation with non-zero constants x, a, and b, which is expressed as:

$$\begin{aligned}\frac{1}{x}+\frac{a}{x^2}+\frac{b}{x^3} = &\frac{1}{x-a+(a^2-b)/x}\\ &+\frac{a^3-2ab+(a^2b-b^2)/x}{x^4-ax^3+(a^2-b)x^2}. \quad \text{(A7)}\end{aligned}$$

If $x = \ln(1/\kappa)$ is much larger than a and b, we can only keep the first term of the right side of equation (A7), and accordingly, equation (A6) will be simplified to

$$\begin{aligned}F_{f\parallel} = 2\pi\mu U_{\parallel}&\left\{\left[\frac{1}{\ln(1/\kappa)}-\frac{3}{2}+\ln 2+\frac{K}{4}\right.\right.\\ &\left.\left.-\left(1-\frac{\pi^2}{12}\right)\Big/\ln(1/\kappa)\right]^{-1}+O\left[\frac{1}{\ln^4(1/\kappa)}\right]\right\}. \quad \text{(A8)}\end{aligned}$$

When $K = 0$, equation (A8) reduces to the classical RFT expression (cf equation (19) in [35]). However, in our work, $\ln(1/\kappa)$ is around 3, and K is

uncertain. Therefore, the approximation of equation (A8) does not work; instead, equation (A6) should be used.

When the body moves perpendicularly to its centerline, resulting in the Stokeslet vector $\mathbf{S}(s) = S_\perp(s)\hat{\mathbf{y}}$, and the relative velocity $\mathbf{U} = U_\perp\hat{\mathbf{y}}$, then equation (A1) is recast as

$$S_\perp(s) = \frac{1}{2\ln\kappa}\left\{U_\perp + S_\perp(s)\left[K_{22} + \ln\left(4s - 4s^2\right) + 1\right] + \int_{-s}^{1-s}\frac{S_\perp(s+\delta) - S_\perp(s)}{|\delta|}\mathrm{d}\delta\right\}. \quad \text{(A9)}$$

The zeroth iterative of equation (A9) is expressed as:

$$S_\perp{}^{(0)}(s) = \frac{U_\perp}{2\ln\kappa}. \quad \text{(A10)}$$

Replacing $S_\perp(s)$ on the right side of equation (A9) with the right-hand side of equation (A10) renders the first iterative of the normal Stokeslet, expressed as:

$$S_\perp{}^{(1)}(s) = \frac{U_\perp}{2\ln\kappa}\left\{1 + \frac{1}{2\ln\kappa}\left[K_{22} + \ln\left(4s - 4s^2\right) + 1\right]\right\}. \quad \text{(A11)}$$

Replacing $S_\perp(s)$ on the right side of equation (A9) with the right-hand side of equation (A11) reaches the second iterative of the normal Stokeslet, expressed as:

$$\begin{aligned} S_\perp{}^{(2)}(s) &= \frac{U_\perp}{2\ln\kappa}\left\{1 + \frac{K_{22}}{2\ln\kappa} + \left(\frac{K_{22}}{2\ln\kappa}\right)^2 + \left(\frac{1}{2\ln\kappa} + \frac{K_{22}}{2\ln^2\kappa}\right)\right. \\ &\quad \times\left[\ln\left(4s - 4s^2\right) + 1\right] + \left[\frac{\ln\left(4s - 4s^2\right) + 1}{2\ln\kappa}\right]^2 \\ &\quad \left. + \int_{-s}^{1-s}\frac{\ln\left[4(s+\delta)(1-s-\delta)\right] - \ln\left(4s - 4s^2\right)}{(2\ln\kappa)^2}\frac{\mathrm{d}\delta}{|\delta|}\right\}. \end{aligned} \quad \text{(A12)}$$

Then the total fluid force normal to the slender body of unit length is expressed, based on equation (2), as:

$$\begin{aligned} F_{f\perp} &= -8\pi\mu\int_0^1 S_\perp{}^{(2)}(s)\,\mathrm{d}s \\ &= -8\pi\mu\frac{U_\perp}{2\ln\kappa}\left\{1 + \frac{K_{22}}{2\ln\kappa} + \left(\frac{K_{22}}{2\ln\kappa}\right)^2\right. \\ &\quad + \left(\frac{1}{2\ln\kappa} + \frac{K_{22}}{2\ln^2\kappa}\right)\int_0^1\left[\ln\left(4s - 4s^2\right) + 1\right]\mathrm{d}s \\ &\quad + \frac{1}{(2\ln\kappa)^2}\int_0^1\left[\ln\left(4s - 4s^2\right) + 1\right]^2\mathrm{d}s + \frac{1}{(2\ln\kappa)^2} \\ &\quad \left.\times\int_0^1\int_{-s}^{1-s}\frac{\ln\left[4(s+\delta)(1-s-\delta)\right] - \ln\left(4s - 4s^2\right)}{|\delta|}\mathrm{d}\delta\mathrm{d}s\right\} \\ &= -4\pi\mu\frac{U_\perp}{\ln\kappa}\left\{1 + \frac{K_{22}}{2\ln\kappa} + \left(\frac{K_{22}}{2\ln\kappa}\right)^2\right. \\ &\quad + \left(\frac{1}{2\ln\kappa} + \frac{K_{22}}{2\ln^2\kappa}\right)(2\ln 2 - 1) + \frac{1}{(2\ln\kappa)^2} \\ &\quad \left.\times\left[4\left(\frac{1}{2} - \ln 2\right)^2 + 4 - \frac{\pi^2}{3}\right] + \frac{1}{(2\ln\kappa)^2}\left(-2.724\times10^{-8}\right)\right\} \\ &= 4\pi\mu U_\perp\left[\frac{1}{\ln(1/\kappa)} + \frac{\frac{1}{2} - \ln 2 - \frac{K_{22}}{2}}{\ln^2(1/\kappa)}\right. \\ &\quad \left. + \frac{\left(\frac{1}{2} - \ln 2 - \frac{K_{22}}{2}\right)^2 + 1 - \frac{\pi^2}{12}}{\ln^3(1/\kappa)}\right]. \end{aligned} \quad \text{(A13)}$$

The normal coefficient of resistive force, i.e. equation (9), can be obtained from equation (A13) by setting $K_{22} = -K$ due to the zero divergence of $\mathbf{K}$. Similarly, equation (A13) can also be simplified under the condition of sufficiently large $\ln(1/\kappa)$, which is expressed as:

$$F_{f\perp} = 4\pi\mu U_\perp\left\{\left[\frac{1}{\ln(1/\kappa)} - \frac{1}{2} + \ln 2 - \frac{K}{2} - \left(1 - \frac{\pi^2}{12}\right)\Big/\ln(1/\kappa)\right]^{-1} + O\left[\frac{1}{\ln^4(1/\kappa)}\right]\right\}. \quad \text{(A14)}$$

When $K = 0$, equation (A14) reduces the classical RFT expression (cf equation (20) in [35]). However, we use equation (A13) in our work because $\ln(1/\kappa)$ is not large, and K is uncertain.

Appendix B. Detailed derivation of the equations of motion based on the bar-joint model

A point P in the ith bar with the distance s from the joint $(i-1)$ has the coordinate $\mathbf{P}_i(s)$ expressed as:

$$\mathbf{P}_i(s) = [x_i + (s-l)\cos\theta_i, y_i + (s-l)\sin\theta_i]^{\mathrm{T}}. \quad \text{(B1)}$$

Note that the coordinates of the head center $\mathbf{P}_0 = (x_0, y_0)^{\mathrm{T}}$ is independent of s, which is be employed to track the trajectory of the microswimmer. Differentiating the right-hand side of equation (B1) with respect to time yields the translational velocity $\mathbf{V}_i(s)$:

$$\mathbf{V}_i(s) = \mathbf{T}_{Vi}(s)\dot{\mathbf{X}}_i = \begin{bmatrix} 1 & 0 & -(s-l)\sin\theta_i \\ 0 & 1 & (s-l)\cos\theta_i \end{bmatrix}\begin{bmatrix} \dot{x}_i \\ \dot{y}_i \\ \dot{\theta}_i \end{bmatrix}, \quad \text{(B2)}$$

where $\mathbf{T}_{Vi}(s)$ is the transformation matrix of velocity for the points in the ith bar.

To simplify the derivation, we first assume that the swimmer suspends in a static fluid field, i.e. $\mathbf{u} = 0$. Hence, the relative velocity $\mathbf{U} = -\mathbf{V}$, and the total fluid forces on a rigid slender body, i.e. equation (7*a*,*b*), are recast to $F_{f_\parallel} = -c_\parallel V_\parallel$ and $F_{f_\perp} = -c_\perp V_\perp$. Based

on the RFT, the resistive coefficients $c_{\parallel}$ and $c_{\perp}$ are assumed to be constant even if the body is flexible and curved, i.e. the tangential and vertical components of local fluid forces $\mathbf{f}_f(s)$ at position s can be formulated as: $f_{f_{\parallel}}(s) = -c_{\parallel} V_{\parallel}(s)$ and $f_{f_{\perp}}(s) = -c_{\perp} V_{\perp}(s)$. Consequently, the tensor of resistive coefficients $\mathbf{C}_i$ for the ith bar based on the CRFT can be expressed as:

$$\mathbf{C}_i = \begin{bmatrix} -c_{\parallel i} & 0 \\ 0 & -c_{\perp i} \end{bmatrix}. \tag{B3}$$

Note that $\mathbf{C}_i$ varies with i because the bar width may vary when considering a tapered flagellum. The fluid forces $\mathbf{f}_{\mathrm{flu}i}(s)$ at position s of the ith bar is then expressed as:

$$\begin{aligned} \mathbf{f}_{\mathrm{flu}i}(s) =& \mathbf{T}_{Ri}^{-1}\left\{\mathbf{C}_i\left[\mathbf{T}_{Ri}\mathbf{V}_i(s)\right]\right\} \\ =& \mathbf{T}_{Ri}^{-1}\mathbf{C}_i\mathbf{T}_{Ri}\mathbf{T}_{Vi}(s)\dot{\mathbf{X}}_i = \mathbf{a}_i(s)\dot{\mathbf{X}}_i, \end{aligned} \tag{B4}$$

where $\mathbf{T}_{Ri} = \begin{bmatrix} \cos\theta_i & \sin\theta_i \\ -\sin\theta_i & \cos\theta_i \end{bmatrix}$ is the transformation matrix of rotation and the 2×3 resistive matrix $\mathbf{a}_i(s)$ depends on the position s of the ith bar. We introduce the unit vectors $\mathbf{e}_1 = (1, 0, 0)^{\mathrm{T}}$, $\mathbf{e}_2 = (0, 1, 0)^{\mathrm{T}}$, and $\mathbf{e}_3 = (0, 0, 1)^{\mathrm{T}}$ to facilitate derivations and the resultant fluid force vector $\mathbf{F}_{\mathrm{flu}i}$ for the ith bar. The latter is given by:

$$\begin{aligned} \mathbf{F}_{\mathrm{flu}i} =& \int_0^{2l}\left[\mathbf{I}_a\mathbf{f}_{\mathrm{flu}i}(s) + \mathbf{P}_i(s) \times \mathbf{f}_{\mathrm{flu}i}(s)\right] \mathrm{d}s \\ =& \left\{\int_0^{2l}\left[\mathbf{I}_a\mathbf{a}_i + \sum_{j=1}^{3}\mathbf{P}_i \times \left(\mathbf{a}_i \cdot \mathbf{e}_j\right) \otimes \mathbf{e}_j\right] \mathrm{d}s\right\}\dot{\mathbf{X}}_i \\ =& \mathrm{A}_i\dot{\mathbf{X}}_i, \end{aligned} \tag{B5}$$

where the operators $\times$ and $\otimes$ indicate cross and outer products of two vectors, respectively, the 3×3 tensor $\mathbf{A}_i$ is the fluid resistive matrix of the ith bar, and the augmented identity matrix $\mathbf{I}_a = \begin{bmatrix} 1 & 0 & 0 \\ 0 & 1 & 0 \end{bmatrix}^{\mathrm{T}}$ is employed to extend the number of rows from 2 to 3 (note that the third component of $\mathbf{F}_{\mathrm{flu}i}$ is the resultant torque about the origin of the coordinate system due to fluid forces). We assume that the hydrodynamic resultant forces and torque on the circular head $\mathbf{F}_{\mathrm{flu}0}$ can be expressed as:

$$\mathbf{F}_{\mathrm{flu}0} = \begin{bmatrix} -c_H & 0 & 0 \\ 0 & -c_H & 0 \\ c_H y_0 & -c_H x_0 & -c_{HR} \end{bmatrix} \begin{bmatrix} \dot{x}_0 \\ \dot{y}_0 \\ \dot{\theta}_0 \end{bmatrix} = \mathbf{A}_0\dot{\mathbf{X}}_0, \tag{B6}$$

where c_H and c_{HR} are coefficients of resistance and are dependent on the head geometry and fluid viscosity [75]. Note that for a 2D FSI simulation, a circular head is a cylinder instead of a sphere. In this case, c_H should be proportional to the thickness of W_z with a coefficient of resistance related to the Reynolds number, expressed as [76]:

$$c_H = \frac{4\pi\mu W_z}{1/2 - \gamma - \ln(\mathrm{Re}/8)}, \tag{B7}$$

where $\gamma \approx 0.577$ is the Euler's constant, and the Reynolds number of the head $\mathrm{Re} = 2\rho V R_H/\mu$. For the micro-swimmer herein, considering the fluid density $\sim 10^3$ kg·m^{-3}, and the terminal velocity $V \sim 10^{-3}$ m·s^{-1}, Re can be estimated to be $2R_H/\mu$. The rotational drag coefficient of the head c_{HR} is determined by [58]:

$$c_{HR} = 4\pi\mu {R_H}^2 W_z. \tag{B8}$$

Then the equilibrium equations for the whole micro-swimmer can be given by

$$\sum_{i=1}^{n}\mathbf{A}_i\dot{\mathbf{X}}_i + \mathbf{A}_0\dot{\mathbf{X}}_0 + \mathbf{F}_0 = \mathbf{0}, \tag{B9}$$

or equation (10).

At the ith joint, the velocities determined from the two connected bars should be equal, i.e. $\mathbf{V}_i(2\,\mathrm{l}) = \mathbf{V}_{i+1}(0)$, which after substituting equation (B2), gives rise to the kinematic constraints:

$$\begin{bmatrix} -\mathbf{T}_{Vi}(2l) & \mathbf{T}_{V(i+1)}(0) \end{bmatrix} \begin{bmatrix} \dot{\mathbf{X}}_i \\ \dot{\mathbf{X}}_{i+1} \end{bmatrix} = \mathbf{0}, \tag{B10}$$

where i runs from 1 to $(n-1)$. Since the first bar and the head are assumed to be rigidly connected, one can obtain the below ODEs in terms of the constraint:

$$\begin{aligned} \dot{\mathbf{X}}_0 =& \mathbf{I}_a\mathbf{V}_1(-R_H) + (\mathbf{e}_3 \otimes \mathbf{e}_3)\dot{\mathbf{X}}_1 \\ =& \left[\mathbf{I}_a\mathbf{T}_{V1}(-R_H) + \mathbf{e}_3 \otimes \mathbf{e}_3\right]\dot{\mathbf{X}}_1 = \mathbf{B}_0\dot{\mathbf{X}}_1. \end{aligned} \tag{B11}$$

For shorthand, equations (B10) and (B11) can be combined as equation (11).

For the moment equilibrium, as demonstrated in figure S1, torques are taken about the origin. The reaction forces at the ith joint F_{Rx} and F_{Ry} can be determined by the balance of forces over the first i bars and the head. The moment equilibrium of the structure before the ith joint leads to the below equations:

$$\begin{aligned} 0 =& M_i + \sum_{j=1}^{i}\left(\mathbf{F}_{\mathrm{flu}j} \cdot \mathbf{e}_3\right) + \left(\mathbf{F}_{\mathrm{flu}0} + \mathbf{F}_0\right) \cdot \mathbf{e}_3 \\ & - \left\{\mathbf{P}_i(2l) \times \left[\left({\mathbf{F}_0}^{\mathrm{T}}\mathbf{I}_a\right)^{\mathrm{T}} + \left({\mathbf{F}_{\mathrm{flu}0}}^{\mathrm{T}}\mathbf{I}_a\right)^{\mathrm{T}}\right.\right. \\ & \left.\left. + \sum_{j=1}^{i}\int_0^{2l}\mathbf{f}_{\mathrm{flu}j}(s)\,\mathrm{d}s\right]\right\} \cdot \mathbf{e}_3, \end{aligned} \tag{B12}$$

where i runs from 1 to $(n-1)$. Substituting equations (B3), (B4), (B9) and (12) into (B12) gives rise

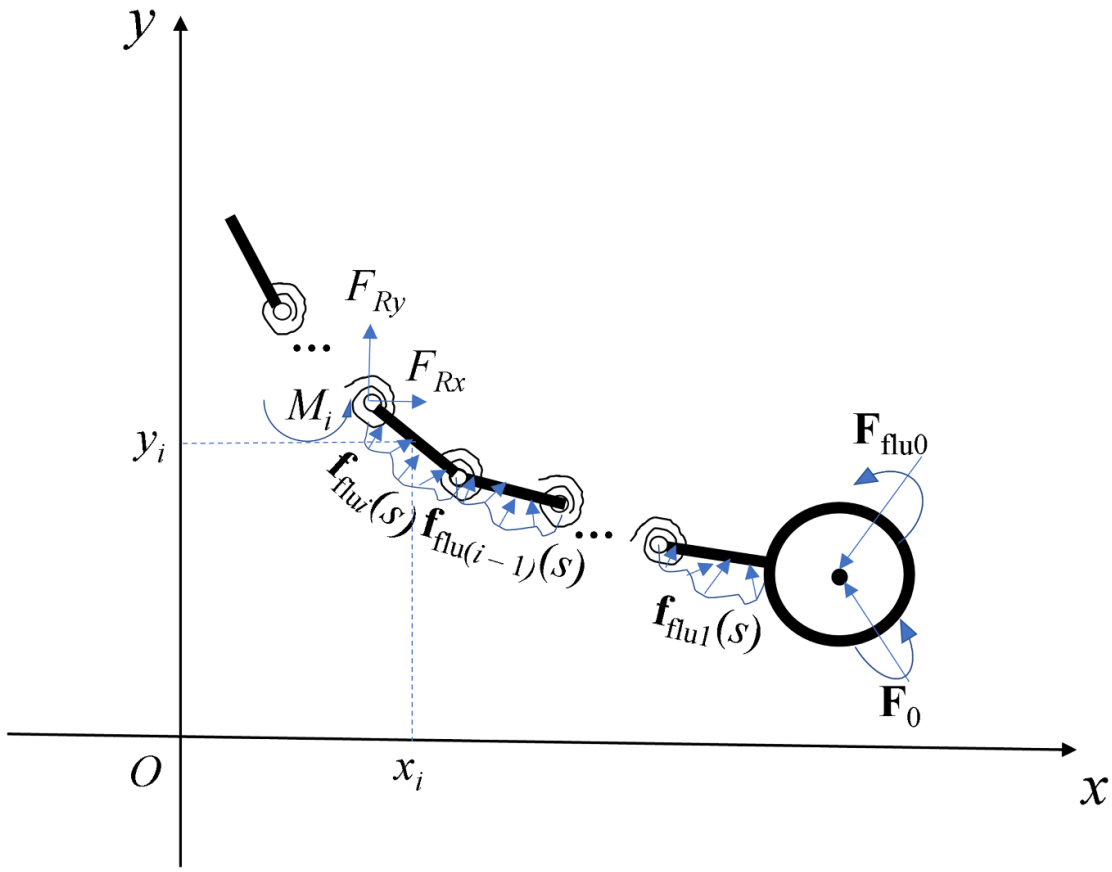

Figure S1. The diagram of force analysis for the bar-joint model.

to the moment equilibrium of the structure, i.e. equation (13).

Finally, combining equations (10)–(13), the governing ODEs of the bar-joint model based on the CRFT can be expressed as equation (14). The equations of motion (equation (14)) are a set of $(3n+3)$ ODEs, in which the velocity vectors are:

$$\dot{\mathbf{X}} = \left[\begin{array}{ccccccc} \dot{\mathbf{X}}_1 & \dot{\mathbf{X}}_2 & \dots & \dot{\mathbf{X}}_i & \dots & \dot{\mathbf{X}}_n \end{array} \right]^{\mathrm{T}}, \tag{B13}$$

where

$$\dot{\mathbf{X}}_i = \left[\begin{array}{ccc} \dot{x}_i & \dot{y}_i & \dot{\theta}_i \end{array} \right]^{\mathrm{T}}, \tag{B14}$$

and the velocity vector of head:

$$\dot{\mathbf{X}}_0 = \left[\begin{array}{ccc} \dot{x}_0 & \dot{y}_0 & \dot{\theta}_0 \end{array} \right]^{\mathrm{T}}. \tag{B15}$$

The 3×3 n resistive matrix of the flagellum is expressed as:

$$\mathbf{A} = \left[\begin{array}{ccccccc} \mathbf{A}_1 & \mathbf{A}_2 & \dots & \mathbf{A}_i & \dots & \mathbf{A}_n \end{array} \right], \tag{B16}$$

where

$$\mathbf{A}_i = \left[\begin{array}{ccc} A_{i11} & A_{i12} & A_{i13} \\ A_{i21} & A_{i22} & A_{i23} \\ A_{i31} & A_{i32} & A_{i33} \end{array} \right], \tag{B17}$$

and the nine components of $\mathbf{A}_i$ are respectively expressed as:

$$\begin{aligned} A_{i11} &= -2l\left(c_{\perp i}\sin^2\theta_i + c_{\parallel i}\cos^2\theta_i\right), \\ A_{i12} &= 2l\left(c_{\perp i} - c_{\parallel i}\right)\sin\theta_i\cos\theta_i, \\ A_{i13} &= 0, \\ A_{i21} &= 2l\left(c_{\perp i} - c_{\parallel i}\right)\sin\theta_i\cos\theta_i, \\ A_{i22} &= -2l\left(c_{\perp i}\cos^2\theta_i + c_{\parallel i}\sin^2\theta_i\right), \\ A_{i23} &= 0, \\ A_{i31} &= 2l\Big[c_{\perp i}\sin\theta_i\left(x_i\cos\theta_i + y_i\sin\theta_i\right) \\ &\quad + c_{\parallel i}\cos\theta_i\left(y_i\cos\theta_i - x_i\sin\theta_i\right)\Big], \\ A_{i32} &= -2l\Big[c_{\perp i}\cos\theta_i\left(x_i\cos\theta_i + y_i\sin\theta_i\right) \\ &\quad + c_{\parallel i}\sin\theta_i\left(x_i\sin\theta_i - y_i\cos\theta_i\right)\Big], \\ A_{i33} &= -\frac{2}{3}l^3 c_{\perp i}. \end{aligned} \tag{B18}$$

The resistive matrix of a head, as given in equation (B6), is expressed as:

$$\mathbf{A}_0 = \left[\begin{array}{ccc} -c_H & 0 & 0 \\ 0 & -c_H & 0 \\ c_H y_0 & -c_H x_0 & -c_{HR} \end{array} \right]. \tag{B19}$$

The matrix of kinematic constraints of neighboring bars is expressed in the form of:

$$\mathbf{T}_V = \begin{bmatrix} -\mathbf{T}_{V1}(2l) & \mathbf{T}_{V2}(0) & \mathbf{0} & \dots & \mathbf{0} & \mathbf{0} \\ \mathbf{0} & -\mathbf{T}_{V2}(2l) & \mathbf{T}_{V3}(0) & \dots & \mathbf{0} & \mathbf{0} \\ \mathbf{0} & \mathbf{0} & -\mathbf{T}_{V3}(2l) & \dots & \mathbf{0} & \mathbf{0} \\ \dots & \dots & \dots & \dots & \dots & \dots \\ \mathbf{0} & \mathbf{0} & \mathbf{0} & \dots & \mathbf{T}_{V(n-1)}(0) & \mathbf{0} \\ \mathbf{0} & \mathbf{0} & \mathbf{0} & \dots & -\mathbf{T}_{V(n-1)}(2l) & \mathbf{T}_{Vn}(0) \end{bmatrix}, \tag{B20}$$

where

$$\mathbf{T}_{Vi}(2l) = \begin{bmatrix} 1 & 0 & -l\sin\theta_i \\ 0 & 1 & l\cos\theta_i \end{bmatrix}, \tag{B21}$$

$$\mathbf{T}_{V(i+1)}(0) = \begin{bmatrix} 1 & 0 & l\sin\theta_{i+1} \\ 0 & 1 & -l\cos\theta_{i+1} \end{bmatrix}. \tag{B22}$$

The $3 \times 3n$ matrix $\mathbf{B}$, obtained from the kinematic constraint between the first bar and the head, is expressed as:

$$\mathbf{B} = \begin{bmatrix} \mathbf{B}_0 & \mathbf{0} & \mathbf{0} & \dots & \mathbf{0} & \mathbf{0} \end{bmatrix}, \tag{B23}$$

where

$$\mathbf{B}_0 = \begin{bmatrix} 1 & 0 & (R_H + l)\sin\theta_1 \\ 0 & 1 & -(R_H + l)\cos\theta_1 \\ 0 & 0 & 1 \end{bmatrix}. \tag{B24}$$

The matrix of torque balance related to the joints $\mathbf{D}$ is expressed in the form as:

$$\mathbf{D} = \begin{bmatrix} \mathbf{D}_{11} & \mathbf{D}_{12} & \mathbf{0} & \dots & \mathbf{0} & \dots & \mathbf{0} \\ \mathbf{D}_{21} & \mathbf{D}_{22} & \mathbf{D}_{23} & \dots & \mathbf{0} & \dots & \mathbf{0} \\ \dots & \dots & \dots & \dots & \dots & \dots & \dots \\ \mathbf{D}_{i1} & \mathbf{D}_{i2} & \mathbf{D}_{i3} & \dots & \mathbf{D}_{ij} & \dots & \mathbf{0} \\ \dots & \dots & \dots & \dots & \dots & \dots & \dots \\ \mathbf{D}_{(n-1)1} & \mathbf{D}_{(n-1)2} & \mathbf{D}_{(n-1)3} & \dots & \mathbf{D}_{(n-1)j} & \dots & \mathbf{D}_{(n-1)n} \end{bmatrix}, \tag{B25}$$

where i runs from 1 to $(n-1)$, and j from 1 to $(i+1)$. The expression of row vector $\mathbf{D}_{ij}$ is dependent on the relation between i and j: when $j < i$, $\mathbf{D}_{ij}$ is expressed as:

$$\mathbf{D}_{ij} = \begin{bmatrix} (x_i + l\cos\theta_i)A_{j21} - (y_i + l\sin\theta_i)A_{j11} - A_{j31} \\ (x_i + l\cos\theta_i)A_{j22} - (y_i + l\sin\theta_i)A_{j12} - A_{j32} \\ (x_i + l\cos\theta_i)A_{j23} - (y_i + l\sin\theta_i)A_{j13} - A_{j33} \end{bmatrix}^{\mathrm{T}}, \tag{B26}$$

when $j = i$, $\mathbf{D}_{ij}$ is expressed as:

$$\mathbf{D}_{ij} = \begin{bmatrix} (x_i + l\cos\theta_i)A_{i21} - (y_i + l\sin\theta_i)A_{i11} - A_{i31} \\ (x_i + l\cos\theta_i)A_{i22} - (y_i + l\sin\theta_i)A_{i12} - A_{i32} \\ (x_i + l\cos\theta_i)A_{i23} - (y_i + l\sin\theta_i)A_{i13} - A_{i33} + \eta(J_i + J_{i+1})/4l \end{bmatrix}^{\mathrm{T}}, \tag{B27}$$

when $j = i + 1$, $\mathbf{D}_{ij}$ is expressed as:

$$\mathbf{D}_{ij} = \begin{bmatrix} 0 \\ 0 \\ -\eta(J_i + J_{i+1})/4l \end{bmatrix}^{\mathrm{T}}. \tag{B28}$$

The matrix of torque balance related to head is expressed as:

$$\mathbf{D}_0 = \begin{bmatrix} \mathbf{D}_{01} \\ \mathbf{D}_{02} \\ \dots \\ \mathbf{D}_{0i} \\ \dots \\ \mathbf{D}_{0(n-1)} \end{bmatrix}, \tag{B29}$$

where the row vector $\mathbf{D}_{0i}$ is expressed as:

$$\mathbf{D}_{0i} = \begin{bmatrix} c_H(y_i + l\sin\theta_i - y_0) \\ c_H(x_0 - x_i - l\cos\theta_i) \\ c_{HR} \end{bmatrix}^{\mathrm{T}}. \tag{B30}$$

The vector of velocity-independent torques is expressed as:

$$\mathbf{F}_E = \begin{bmatrix} F_{E1} & F_{E2} & \dots & F_{Ei} & \dots & F_{E(n-1)} \end{bmatrix}^{\mathrm{T}}, \tag{B31}$$

where the ith component F_{Ei} is expressed as:

$$F_{Ei} = E\frac{J_i + J_{i+1}}{2}\frac{\theta_{i+1} - \theta_i}{2l} + (y_i + l\sin\theta_i - y_H)F_{\mathrm{extx}} + (x_H - x_i - l\cos\theta_i)F_{\mathrm{exty}} + \tau_{\mathrm{ext}}. \tag{B32}$$

When a micro-swimmer suspends in a non-static fluid circumstance, e.g. in a plane acoustic field with the velocity of fluid at the location of the ith bar $\mathbf{u}_i = (u_{ix}, u_{iy}, 0)^{\mathrm{T}}$ (it is $\mathbf{u}_0$ at the head), then for the relative velocity $\mathbf{U} = \mathbf{u} - \mathbf{V}$, the equations of local fluid forces will be recast as $f_{f_\parallel}(s) = c_\parallel u_\parallel(s) - c_\parallel V_\parallel(s)$ and $f_{f_\perp}(s) = c_\perp u_\perp(s) - c_\perp V_\perp(s)$. Eventually, the governing equations equation (14) will maintain the form except that the right-hand side non-homogenous terms must be revised to:

$$\mathbf{F}_0 = \begin{bmatrix} F_{\mathrm{extx}} \\ F_{\mathrm{exty}} \\ \tau_{\mathrm{ext}} + x_0F_{\mathrm{exty}} - y_0F_{\mathrm{extx}} - c_Hy_0u_{0x} + c_Hx_0u_{0y} \end{bmatrix} - \sum_{i=1}^{n}\mathbf{A}_i\mathbf{u}_i, \tag{B33}$$

$$\begin{aligned} F_{Ei} = {} & E\frac{J_i + J_{i+1}}{2}\frac{\theta_{i+1} - \theta_i}{2l} + (y_i + l\sin\theta_i - y_H)F_{\mathrm{extx}} \\ & + (x_H - x_i - l\cos\theta_i)F_{\mathrm{exty}} + \tau_{\mathrm{ext}} \\ & + \sum_{j=1}^{i} u_{ix}\Big[(x_i + l\cos\theta_i)A_{j21} - (y_i + l\sin\theta_i)A_{j11} - A_{j31}\Big] + u_{0x}c_H(y_i + l\sin\theta_i - y_0) \\ & + \sum_{j=1}^{i} u_{iy}\Big[(x_i + l\cos\theta_i)A_{j22} - (y_i + l\sin\theta_i)A_{j12} - A_{j32}\Big] + u_{0y}c_H(x_0 - x_i - l\cos\theta_i). \end{aligned} \tag{B34}$$

The Buckingham π theorem [63] is employed for nondimensionalization. We take the half-length of each bar l, the period of acoustic actuation $T = 1/f_r$, and the fluid viscosity μ as repeating variables, then the following non-dimensional terms are introduced:

$$\begin{aligned} &\tilde{x} = \frac{x}{l}, \tilde{u} = \frac{Tu}{l}, \tilde{t} = \frac{t}{T}, \tilde{s} = \frac{s}{l}, \tilde{J} = \frac{J}{l^4}, \tilde{E} = \frac{TE}{\mu}, \\ &\tilde{\eta} = \frac{\eta}{\mu}, \tilde{c} = \frac{c}{\mu}, \tilde{c}_H = \frac{c_H}{l\mu}, \tilde{c}_{HR} = \frac{c_{HR}}{l^3\mu}, \tilde{R}_H = \frac{R_H}{l}, \\ &\tilde{F} = \frac{TF}{\mu l^2}, \tilde{\tau} = \frac{T\tau}{\mu l^3}. \end{aligned} \tag{B35}$$

The dimensionless governing equations equation (14) can then be reached, where the three variables l, T, and μ become unity, and other physical quantities can be directly replaced according to equation (B35).

Appendix C. Convergence analyses of the bar-joint model

Here we show an example of the convergence analysis of the bar-joint model. For the convenience of comparisons, all the geometric and material parameters have the same values as those in the 1D classical continuum model reported in [24] in which the cross-section of the tapered flagellum is circular with the largest diameter $W_{y0} = 25$ μm and the tapering index $\lambda = 0.9$. Hence, for the bar-joint model, if we take the diameter at position $\mathbf{P}_i(0)$ of a continuum flagellum as the diameter of the ith bar, i.e. W_{yi}, of a bar-joint flagellum, then W_{yi} can be derived given by:

$$W_{y_i} = W_{y_0}\left[1 - \lambda\frac{2l(i-1)}{L}\right], \tag{C1}$$

where i is from 1 to n. The head is assumed to be a sphere with a radius of $R_H = 25$ μm, and the effect of the spherical head on locomotion is accounted for by the coefficient of resistance c_H given below as reported in [24],

$$c_H = 6\pi\mu R_H. \tag{C2}$$

Other parameters in the bar-joint model are: $K = 0$ (i.e. for the circular cross-section, the CRFT reduces to the RFT), $c_{HR} = 0$ for eliminating the resistive effect of head rotation, $\mathbf{u} = 0$, $F_{\mathrm{extx}} = 0$, $F_{\mathrm{exty}} = F_a\cos\omega t$, $\tau_{\mathrm{ext}} = 0$, $f_r = 4600$ Hz, $L = 180$ μm, $E = 10$ MPa, $\eta = 1730$ Pa·s, $\mu = 1$ Pa·s, and $F_a = 344$ μN to make $A_{\mathrm{amp}} = 20$ μm.

For the bar-joint model of the AFMS with a head ($R_H = 25$ μm), we solve the governing ODEs, i.e. equation (14), by using the built-in solver *ode15s* in MATLAB [64]. The number of bars n varies from 2 to 60, and V_{ave} is the position change of the head in the fifth period times f_r. The result of V_{ave} increase with n and levels off (with fluctuations) when $n > 20$, as illustrated in figure S2. Note that the analytical result in [24] is ~350 μm·s^{-1} when $A_{\mathrm{amp}} = 20$ μm. The converged result of the bar-joint model is ~260 μm·s^{-1}, 25% smaller from the analytical result in [24]. Such a deviation is in accordance with the expectation (see discussions in [31, 37]) because the 1D analytical model cannot involve the effect of rigid-body rotation which greatly affects the locomotion. Other factors, such as the ignorance of inextensibility and large deflection, also contribute substitutionally to the error of the 1D analytical model.

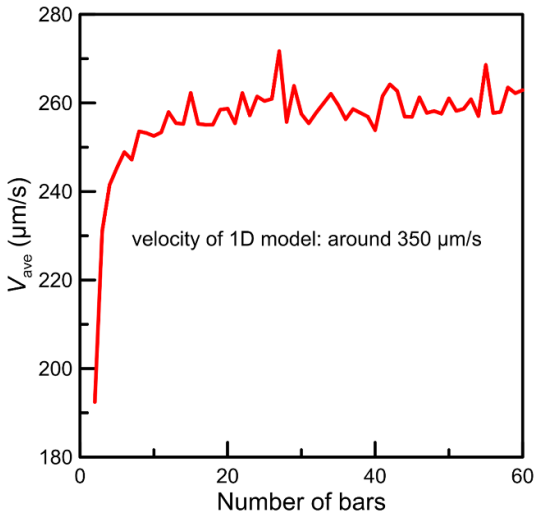

Figure S2. The convergence analysis of the bai-joint model in terms of the number of bars with parameters identical to results of figure 10(d) in [24], i.e. the terminal velocity is around 350 μm·s^{-1} when amplitude is 20 μm.

ORCID iDs

Jinan Liu https://orcid.org/0000-0002-9511-4881
Yiqiang Fu https://orcid.org/0000-0003-3775-1660
Xiongjun Liu https://orcid.org/0000-0002-1663-4636
Haihui Ruan https://orcid.org/0000-0002-9233-8820

References

[1] Abbott J J, Nagy Z, Beyeler F and Nelson B J 2007 Robotics in the small, part I: microbotics *IEEE Robot. Autom. Mag.* **14** 92–103
[2] Baker R, Brooks A M and Sen A 2019 Designing Proteus: engineering form and function for microrobotics *Robotic Systems and Autonomous Platforms* (Amsterdam: Elsevier) pp 85–108
[3] Feynman R 1959 There is plenty of room at the bottom: an invitation to enter a new field of physics *Lecture at American Physical Society Meeting* (available at: www.zyvex.com/nanotech/feynman.html)
[4] Toumey C 2008 The literature of promises *Nat. Nanotechnol.* **3** 180
[5] Feng J and Cho S K 2014 Mini and micro propulsion for medical swimmers *Micromachines* **5** 97–113
[6] Liu J, Fu Y, Liu X and Ruan H 2021 Theoretical perspectives on natural and artificial micro-swimmers *Acta Mech. Solida Sin.* **34** 783–809
[7] Dijkink R, Van Der Dennen J, Ohl C and Prosperetti A 2006 The 'acoustic scallop': a bubble-powered actuator *J. Micromech. Microeng.* **16** 1653
[8] Bertin N, Spelman T A, Stephan O, Gredy L, Bouriau M, Lauga E and Marmottant P 2015 Propulsion of bubble-based acoustic microswimmers *Phys. Rev. Appl.* **4** 064012
[9] Wang W, Castro L A, Hoyos M and Mallouk T E 2012 Autonomous motion of metallic microrods propelled by ultrasound *ACS Nano* **6** 6122–32
[10] Li T, Li J, Zhang H, Chang X, Song W, Hu Y, Shao G, Sandraz E, Zhang G and Li L 2016 Nanorobots: magnetically propelled fish-like nanoswimmers (small 44/2016) *Small* **12** 6045
[11] Zhang L, Abbott J J, Dong L, Kratochvil B E, Bell D and Nelson B J 2009 Artificial bacterial flagella: fabrication and magnetic control *Appl. Phys. Lett.* **94** 064107
[12] Schuerle S, Pané S, Pellicer E, Sort J, Baró M D and Nelson B J 2012 Helical and tubular lipid microstructures that are electroless-coated with CoNiReP for wireless magnetic manipulation *Small* **8** 1498–502
[13] Ahmed D, Baasch T, Jang B, Pane S, Dual J and Nelson B J 2016 Artificial swimmers propelled by acoustically activated flagella *Nano Lett.* **16** 4968–74
[14] Kaynak M, Ozcelik A, Nourhani A, Lammert P E, Crespi V H and Huang T J 2017 Acoustic actuation of bioinspired microswimmers *Lab Chip* **17** 395–400
[15] Lauga E and Powers T R 2009 The hydrodynamics of swimming microorganisms *Rep. Prog. Phys.* **72** 096601
[16] Sitti M, Ceylan H, Hu W, Giltinan J, Turan M, Yim S and Diller E 2015 Biomedical applications of untethered mobile milli/microrobots *Proc. IEEE* **103** 205–24
[17] Chen X Z, Jang B, Ahmed D, Hu C, De Marco C, Hoop M, Mushtaq F, Nelson B J and Pané S 2018 Small-scale machines driven by external power sources *Adv. Mater.* **30** 1705061
[18] Sánchez S, Soler L and Katuri J 2015 Chemically powered micro-and nanomotors *Angew. Chem., Int. Ed.* **54** 1414–44
[19] Ni M, Leung M K, Leung D Y and Sumathy K 2007 A review and recent developments in photocatalytic water-splitting using TiO_2 for hydrogen production *Renew. Sustain. Energy Rev.* **11** 401–25
[20] Saito K, Iwata K, Ishihara Y, Sugita K, Takato M and Uchikoba F 2016 Miniaturized rotary actuators using shape memory alloy for insect-type MEMS microrobot *Micromachines* **7** 58
[21] Zhou H, Mayorga-Martinez C C, Pané S, Zhang L and Pumera M 2021 Magnetically driven micro and nanorobots *Chem. Rev.* **121** 4999–5041
[22] Rao K J, Li F, Meng L, Zheng H, Cai F and Wang W 2015 A force to be reckoned with: a review of synthetic microswimmers powered by ultrasound *Small* **11** 2836–46
[23] Mohanty S, Khalil I S and Misra S 2020 Contactless acoustic micro/nano manipulation: a paradigm for next generation applications in life sciences *Proc. R. Soc.* A **476** 20200621
[24] Liu J and Ruan H 2020 Modeling of an acoustically actuated artificial micro-swimmer *Bioinsp. Biomim.* **15** 036002
[25] Lighthill J 1976 Flagellar hydrodynamics *SIAM Rev.* **18** 161–230
[26] Purcell E M 1977 Life at low Reynolds number *Am. J. Phys.* **45** 3–11
[27] Taylor G I 1951 Analysis of the swimming of microscopic organisms *Proc. R. Soc.* A **209** 447–61
[28] Ovchinnikov M, Zhou J and Yalamanchili S 2014 Acoustic streaming of a sharp edge *J. Acoust. Soc. Am.* **136** 22–29
[29] Kaynak M, Ozcelik A, Nama N, Nourhani A, Lammert P E, Crespi V H and Huang T J 2016 Acoustofluidic actuation of *in situ* fabricated microrotors *Lab Chip* **16** 3532–7
[30] Spagnolie S E and Lauga E 2012 Hydrodynamics of self-propulsion near a boundary: predictions and accuracy of far-field approximations *J. Fluid Mech.* **700** 105–47
[31] Rorai C, Zaitsev M and Karabasov S 2019 On the limitations of some popular numerical models of flagellated microswimmers: importance of long-range forces and flagellum waveform *R. Soc. Open Sci.* **6** 180745
[32] Hancock G 1953 The self-propulsion of microscopic organisms through liquids *Proc. R. Soc.* A **217** 96–121
[33] Newman J N 1964 A slender-body theory for ship oscillations in waves *J. Fluid Mech.* **18** 602–18
[34] Cox R 1970 The motion of long slender bodies in a viscous fluid part 1. General theory *J. Fluid Mech.* **44** 791–810
[35] Keller J B and Rubinow S I 1976 Slender-body theory for slow viscous flow *J. Fluid Mech.* **75** 705–14
[36] Koens L and Lauga E 2018 The boundary integral formulation of stokes flows includes slender-body theory *J. Fluid Mech.* **850** R1

[37] Rodenborn B, Chen C-H, Swinney H L, Liu B and Zhang H 2013 Propulsion of microorganisms by a helical flagellum *Proc. Natl Acad. Sci.* **110** E338–47
[38] Zhang T and Goldman D I 2014 The effectiveness of resistive force theory in granular locomotion *Phys. Fluids* **26** 101308
[39] Machin K 1958 Wave propagation along flagella *J. Exp. Biol.* **35** 796–806
[40] Wiggins C H and Goldstein R E 1998 Flexive and propulsive dynamics of elastica at low Reynolds number *Phys. Rev. Lett.* **80** 3879
[41] Yu T S, Lauga E and Hosoi A 2006 Experimental investigations of elastic tail propulsion at low Reynolds number *Phys. Fluids* **18** 091701
[42] Singh T S and Yadava R 2017 Effect of tapering on elastic filament microswimming under planar body actuation *Biomed. Phys. Eng. Express* **4** 015019
[43] Yang T-Z, Ji S, Yang X-D and Fang B 2014 Microfluid-induced nonlinear free vibration of microtubes *Int. J. Eng. Sci.* **76** 47–55
[44] Al-Bdor B, Sinawi A and Hamdan M N 2002 Nonlinear dynamic model of an inextensible rotating flexible arm supported on flexible base *J. Sound Vib.* **251** 767–81
[45] Friedrich B M, Riedel-Kruse I H, Howard J and Jülicher F 2010 High-precision tracking of sperm swimming fine structure provides strong test of resistive force theory *J. Exp. Biol.* **213** 1226–34
[46] Saggiorato G, Alvarez L, Jikeli J F, Kaupp U B, Gompper G and Elgeti J 2017 Human sperm steer with second harmonics of the flagellar beat *Nat. Commun.* **8** 1–9
[47] Alouges F, DeSimone A, Giraldi L and Zoppello M 2015 Can magnetic multilayers propel artificial microswimmers mimicking sperm cells? *Soft Robot.* **2** 117–28
[48] Pak O S, Lauga E, Duprat C and Stone H 2015 Theoretical models of low-Reynolds-number locomotion *Fluid-Structure Interactions in Low-Reynolds-Number Flows* (London: Royal Society of Chemistry) pp 100–67
[49] Dowell E and McHugh K 2016 Equations of motion for an inextensible beam undergoing large deflections *J. Appl. Mech.* **83** 051007
[50] Moreau C, Giraldi L and Gadêlha H 2018 The asymptotic coarse-graining formulation of slender-rods, bio-filaments and flagella *J. R. Soc. Interface* **15** 20180235
[51] Curatolo M and Teresi L 2016 Modeling and simulation of fish swimming with active muscles *J. Theor. Biol.* **409** 18–26
[52] Germann P, Menshykau D, Tanaka S and Iber D 2012 Simulating organogenesis in COMSOL (arXiv:1202.0428)
[53] Cordovilla F, García-Beltrán Á, Garzón M, Muñoz D A and Ocaña J L 2018 Numerical-experimental study of the consolidation phenomenon in the selective laser melting process with a thermo-fluidic coupled model *Materials* **11** 1414
[54] Kadry H, Wadnap S, Xu C and Ahsan F 2019 Digital light processing (DLP) 3D-printing technology and photoreactive polymers in fabrication of modified-release tablets *Eur. J. Pharm. Sci.* **135** 60–67
[55] Batchelor G K 1970 Slender-body theory for particles of arbitrary cross-section in stokes flow *J. Fluid Mech.* **44** 419–40
[56] Borker N S and Koch D L 2019 Slender body theory for particles with non-circular cross-sections with application to particle dynamics in shear flows *J. Fluid Mech.* **877** 1098–133
[57] Yang K, Sun P, Wang L, Xu J and Zhang L 2016 Modeling and simulations for fluid and rotating structure interactions *Comput. Methods Appl. Mech. Eng.* **311** 788–814
[58] Chwang A T and Wu T Y-T 1975 Hydromechanics of low-Reynolds-number flow. Part 2. Singularity method for stokes flows *J. Fluid Mech.* **67** 787–815
[59] Odegard G, Gates T and Herring H 2005 Characterization of viscoelastic properties of polymeric materials through nanoindentation *Exp. Mech.* **45** 130–6
[60] Lei Y, Adhikari S and Friswell M 2013 Vibration of nonlocal Kelvin–Voigt viscoelastic damped Timoshenko beams *Int. J. Eng. Sci.* **66** 1–13
[61] Ghayesh M H 2019 Viscoelastic dynamics of axially FG microbeams *Int. J. Eng. Sci.* **135** 75–85
[62] Ghayesh M H, Farokhi H and Hussain S 2016 Viscoelastically coupled size-dependent dynamics of microbeams *Int. J. Eng. Sci.* **109** 243–55
[63] Buckingham E 1914 On physically similar systems; illustrations of the use of dimensional equations *Phys. Rev.* **4** 345
[64] Kuhn L M, Russell S, Boudreaux M, Gaboury J and Maulding B 2019 Development of a rapid first-order differential equation solver for stiff systems *Proc. of the Int. Conf. on Scientific Computing (CSC)* (The Steering Committee of The World Congress in Computer Science, Computer …)
[65] Voß J and Wittkowski R 2022 Orientation-dependent propulsion of triangular nano-and microparticles by a traveling ultrasound wave *ACS Nano* **16** 3604–12
[66] Curtis F G, Ekici K and Freels J D 2011 Fluid-structure interaction for coolant flow in research-type nuclear reactors *Comsol Conf.* (https://doi.org/10.1590/s0102-86502011000300008)
[67] Christian J T and Boehmer J W 1970 Plane strain consolidation by finite elements *J. Soil Mech. Found. Div.* **96** 1435–57
[68] Winslow A M 1966 Numerical solution of the quasilinear Poisson equation in a nonuniform triangle mesh *J. Comput. Phys.* **1** 149–72
[69] Dreyfus R, Baudry J, Roper M L, Fermigier M, Stone H A and Bibette J 2005 Microscopic artificial swimmers *Nature* **437** 862–5
[70] Shi C, Zhao R, Long Y, Yang S, Wang Y, Chen H, Ren J and Zhang X 2019 Observation of acoustic spin *Natl Sci. Rev.* **6** 707–12
[71] Huang H-W, Uslu F E, Katsamba P, Lauga E, Sakar M S and Nelson B J 2019 Adaptive locomotion of artificial microswimmers *Sci. Adv.* **5** eaau1532
[72] Kumar C S and Mohammad F 2011 Magnetic nanomaterials for hyperthermia-based therapy and controlled drug delivery *Adv. Drug. Deliv. Rev.* **63** 789–808
[73] Schenck J F 1996 The role of magnetic susceptibility in magnetic resonance imaging: MRI magnetic compatibility of the first and second kinds *Med. Phys.* **23** 815–50
[74] Nama N, Huang P-H, Huang T J and Costanzo F 2014 Investigation of acoustic streaming patterns around oscillating sharp edges *Lab Chip* **14** 2824–36
[75] Duprat C and Shore H A 2015 *Fluid-structure Interactions in Low-Reynolds-Number Flows* (London: Royal Society of Chemistry)
[76] Huner B and Hussey R 1977 Cylinder drag at low Reynolds number *Phys. Fluids* **20** 1211–8